Electromagnetic Science
vol. 1, no. 3, 0030101, September 2023
https://doi.org/10.23919/emsci.2022.0010

Review

Regulation and Control of Electromagnetic Field in Radio-Frequency Circuits and Systems

Kaixue Ma

Tianjin Key Laboratory of Imaging and Sensing Microelectronic Technology, School of Microelectronics, Tianjin University, Tianjin 300072, China

Corresponding author: Kaixue Ma, Email: makaixue@tju.edu.cn.
Received November 3, 2022; Accepted August 21, 2023; Published Online September 20, 2023.

Abstract — Since the first demonstrations of radio-frequency (RF) circuits, the physics of the electromagnetic (EM) field and its regulation and control with codesigned circuits, have become essential competencies of RF circuit designers. Leveraging advanced regulation or control methods, numerous high-performance circuits have been developed at RF and millimeter-wave (mm-wave) frequencies. Three main methods of electromagnetic regulation have been widely utilized, namely, the separation of electric and magnetic coupling paths, the manipulation of electromagnetic energy through the coupling of multiple tanks or multiple resonators, and the regulation of electromagnetic fields in air cavities or meta-substrates. The separated coupling paths of electric and magnetic fields provide guidance for designing a high-performance filter topology with a quasielliptical response through additional zeros. The manipulation of the EM field through electrical and magnetic intercouplings of multitanks or multiresonators, such as are used in oscillators, power amplifiers (PAs), etc., results in remarkable power efficiency, size reduction, and wide bandwidth. The regulation of electromagnetism through an air cavity, patterned substrate, or metasubstrate reduces dielectric losses and size, especially when using a substrate integrated suspended line (SISL) platform. Many excellent circuits have been reported based on SISL with low loss, high integration, and self-packaging. Here, we present state-of-the-art cases that demonstrate the benefits of EM field regulation and control.

Keywords — Electromagnetic, Mixed coupling, Multiresonators and multitanks, Patterned substrate and metasubstrate, Radio frequency circuits, Regulation and control, Separate electronic and magnetic coupling paths, Substrate integrated suspended line.

Citation — Kaixue Ma, "Regulation and Control of Electromagnetic Field in Radio-Frequency Circuits and Systems," *Electromagnetic Science*, vol. 1, no. 3, article no. 0030101, 2023. doi: 10.23919/emsci.2022.0010.

I. Introduction

With the advancement of wireless communication technology and radio frequency (RF) systems, increasing demands for miniaturization, low loss, and low cost are prompted for integrated circuits and systems with higher performance and compact size. Recently, various technologies for electromagnetic (EM) control in radio frequency circuits has been extensively studied by our group and other researchers. Many circuits operating in RF or microwave regimes have seen improved performance using electromagnetic regulation and control. For example, the control technology in [1] helped to achieve a low insertion loss and small size, as well as controllable transmission zeros (TZs) for the filter design. Additionally, in [2], an enhanced quality-factor (Q-factor) and wide tuning range were performed by introducing electromagnetic control theory for RF ICs. This type of recently developed technology consists of the separation and regulation of electric and magnetic coupling paths, the regulation and control of electromagnetic energy, and electromagnetic control in the medium or substrate.

Commonly implemented methods of separating electric and magnetic coupling paths (SEMCP) filter topology, as shown in Figure 1(a), include physical separation and equivalent separation in electric, i.e., in equivalent or equation. The separation of physical electric and magnetic coupling paths offers the benefits of simplifying the design, intuitive analysis, and separate control of TZs. Equivalent electronic and magnetic coupling paths can provide instructions and guidance to the filter designs according to the equations on the required positions of TZs, return loss, and more. Regarding the regulation and control of electromagnetic energy in EM coupling proposed in [2], as shown in Figure 1(b), this approach can be conducted by electrical coupling, magnetic coupling regulation and control, and mixed electromagnetic techniques that treat the coupled capacitor, inductors or both as equivalent to an electric or magnetic or electromagnetic energy storage device. This combination offers outstanding advantages for silicon-based circuits and systems, such as an enhanced Q-factor, a wide tuning range, a remarkable figure-of-merit (FoM), considerable efficiency and linearity, and a reduced core

area [2]–[11].

To regulate the electromagnetic field effect for reducing loss and minimizing size, the air cavity, embedded medium, and metasubstrate electromagnetic regulation techniques proposed in [12] are introduced to manipulate the electromagnetic wave, as shown in Figure 1(c). The concept of quasiplanar circuits with embedded air cavities, patterned substrate, or metasubstrate is introduced. Compared with traditional planar circuits where electromagnetic energy is mostly confined in substrates, circuits with embedded air cavities, patterned substrates, or metasubstrates, especially those using substrate integrated suspended line (SISL) platforms, feature lower dielectric loss. Many circuits designed based on the SISL platform of different types of transmission lines possess the merits of low dielectric loss, high efficiency, low cost, high integration, and self-

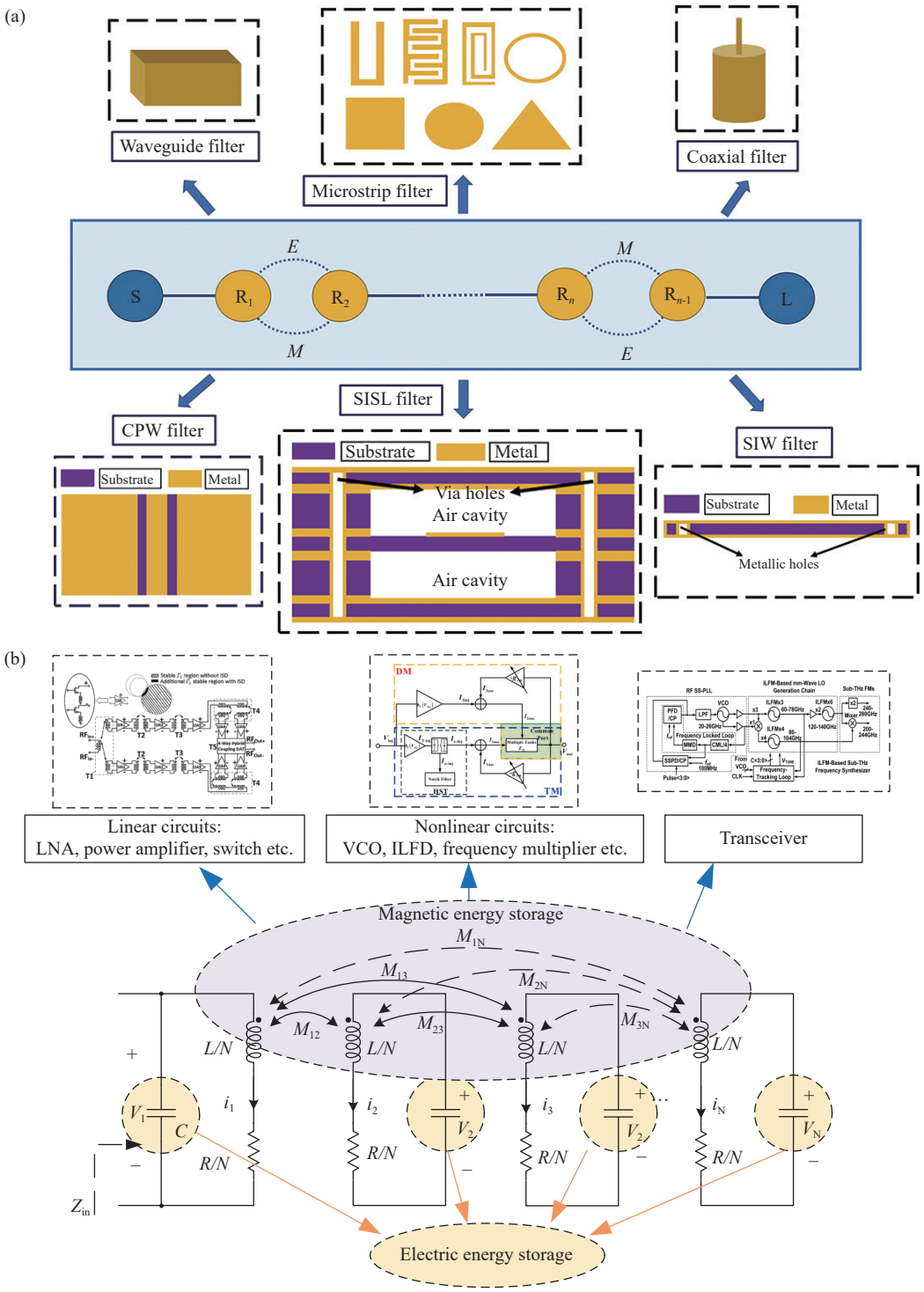

Figure 1 (to be continued)

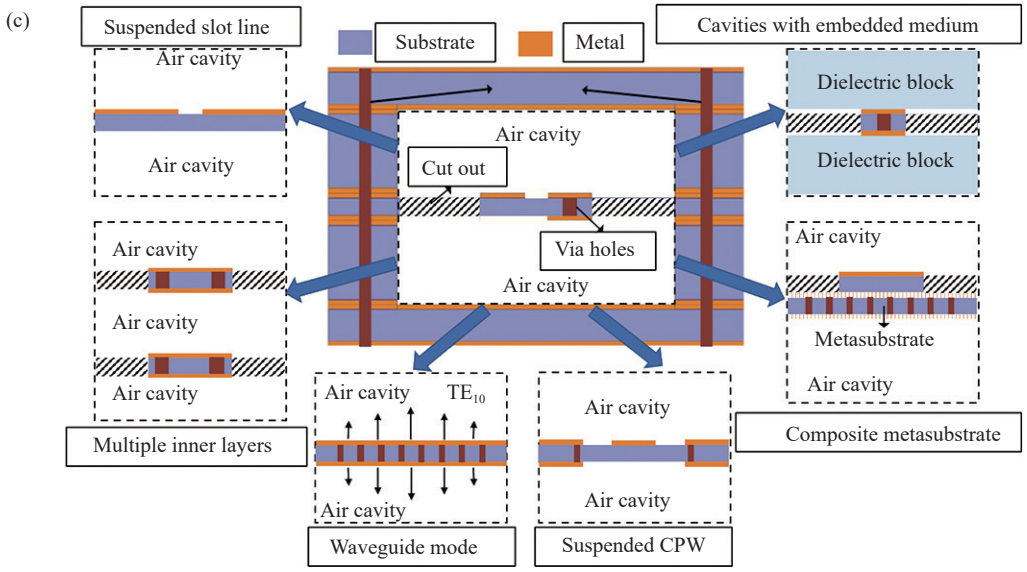

Figure 1 The concept of three methods of regulating and controlling of electromagnetic field in circuits. (a) SEMCP topology and its applications [1]; (b) The regulation and control of electromagnetic energy storage in coupling [2]; (c) The regulation of electromagnetic field in the metasubstrate or air cavity [12], [13]. (continued)

packaging [13]–[30]. To expand the advantages of SISL, several EM regulation methods have been presented to further reduce the loss of substrate and metal, such as double-sided interconnected strip line (DSISL) technology [16], patterned substrates [16], and multiple inner boards [26]. Several methods are introduced to miniaturize the circuit designs, such as loading dielectric blocks with high dielectric constant material, quasilumped elements, and metasubstrate [30]–[34].

The remainder of this article is organized as follows. Section II introduces the theory of separate electric and magnetic coupling paths, combined with analyzing the basic circuits and application cases. Section III discusses the regulation technique of electromagnetic energy in multi-tank circuits, including principles and some circuit designs with enhanced performance. Section IV demonstrates the regulation of EM in air cavities, patterned substrates, loaded dielectric substrates, or metasurface electromagnetics, consisting of theories, guidance for utilizing this technology, and some specific improved methods applied to circuit design. The conclusion summarizes three main kinds of regulation and control technologies for EM, presenting the advantages of applying this newly developed technology.

II. Separating Electric and Magnetic Coupling Path Regulation Theory and Circuits

1. Overview of the SEMCP topology

In recent years, the demand for available frequency channels has continuously increased, which results in more stringent standards for high-performance microwave bandpass filters (BPFs) used in communication systems. Research on BPFs has long been one of the key directions in microwave fields. Direct-coupled microwave BPFs and cross-coupled BPFs [35] were introduced in the early 1950s; since then, much effort has focused on the synthesis and design of BPFs with advanced topologies. Recently, as a promising method to achieve high-performance filter responses, the SEMCP topology proposed by Ma in [1] in the filter synthesis and design process has received significant attention.

Regarding the EM regulation theory of the separating electric and magnetic coupling paths in circuits, two main methods have been implemented thus far, namely, physical path separation and equivalent electric and magnetic coupling path separation. The mechanism of physical path separation is mainly the introduction of two or even more parallel paths in physical space, i.e., an electric coupling path and a magnetic coupling path, and additional TZs can be generated through the EM coupling canceling between the paths. In general, the electric coupling path can be realized by an equivalent capacitive element, while the magnetic coupling path can be realized by an inductive element. Using this method can be more intuitive to reflect the main spatial distribution of the electric and magnetic coupling paths, so it offers the advantages of easy design, simple analysis, and flexible control of TZs and loading effect for size reduction. Equivalent electric and magnetic coupling separation path theory is based on preset indicators, such as the position of TZs, return loss, out-of-band rejection, and other information, to determine the structure of the filter. This approach is also divided into two methods: the first is to optimize the circuit directly based on the coupling matrix, and the second is to synthesize it in the low-pass domain and then convert it to the bandpass domain. That first approach relies on the cost function, and the second relies on rotating and scaling the transformation of the low-pass prototype. For example, we can introduce the separating electric and magnetic coupling path regulation theory in the commonly used cascaded triplet (CT), cascaded quadruplet

(CQ), and other cascade topologies to generate more TZs, thus effectively improving the filter selectivity.

2. Theory and applications in filters

As a promising method to produce flexible TZs, we have studied the underlying synthesis theory and then implemented SEMCP in various circuits. As an example, Figure 2(a) shows a second-order microstrip bandpass filter using the fundamental SEMCP block, which offers two independently controlled electric and magnetic coupling paths. The relationship between the coupling coefficients, electrical coupling, and magnetic coupling can be established using even-odd modes analysis, and the coupling between the two modes can be described by a separate coupling parameter C, as shown in equation (1).

$$C = \frac{\omega_o^2 - \omega_e^2}{\omega_o^2 + \omega_e^2} = F(Y_c L_m - C_m Z_c) = M - E \tag{1}$$

where

$$F = \frac{4(A + Y_c L_m + Z_c C_m)}{(2Y_c L_m + A)^2 + (2Z_c C_m + A)^2} \tag{2}$$

$$A = \frac{\sqrt{\varepsilon_{re}}(l_1 + l_2)}{c} \tag{3}$$

$$M = F Y_c L_m \tag{4}$$

$$E = F Z_c C_m \tag{5}$$

$$\beta_e = \frac{\omega_e \sqrt{\varepsilon_{re}}}{c} \tag{6}$$

where β_e is the propagation constant at the even-mode resonance angular frequency ω_e.

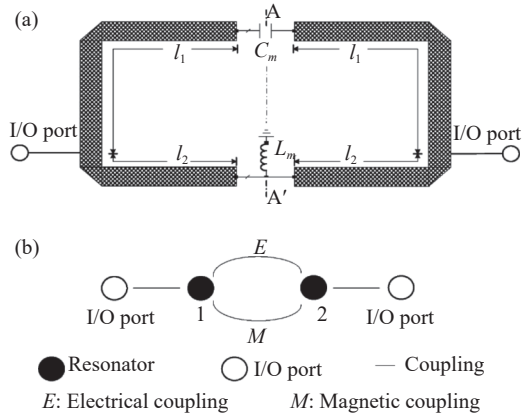

Figure 2 Proposed second-order filter configuration and the topology. (a) Configuration with lump coupling elements; (b) Filter topology [1].

The even-mode resonant angular frequency can be given by

$$\omega_e = \frac{\pi}{2(2L_m Y_c + A)} \tag{7}$$

The odd-mode resonant angular frequency can be determined by

$$\omega_o = \frac{\pi}{2(2C_m Z_c + A)} \tag{8}$$

where L_m and C_m are lumped elements. We can observe that the coupling coefficients of the proposed SEMCP are developed by two separate parts, i.e., magnetic coupling M and electric coupling E, and the two coupling paths are dependent on one another and have canceling effects. c denotes the speed of light in free space, and $Z_c = 1/Y_c$ is the characteristic impedance of the resonator. For a small L_m or C_m, $l_1 + l_2 \approx \lambda_g/4$.

Figure 2(b) shows the responses of the presented second-order BPF using SEMCP. As shown, by selecting a different dominant coupling path and coupling element values, the filter response could be totally regulated. The design of narrow bandwidth BPFs requires a reduced coupling coefficient, which can benefit from the canceling effects in two coupling paths. Numerous excellent works on electromagnetic regulation of planar circuits by separating electric and magnetic coupling paths have been presented and have achieved favorable performance in terms of compact size, low losses, etc. In [1], the concept of the SEMCP and the topology (shown in Figure 2) was proposed, and the coupling mechanism was analyzed based on the equivalent electric and magnetic path separation.

Figure 3(a) illustrates the impact of the coupling elements (L_m and C_m) in the two coupling paths on the filter when magnetic coupling is prominent. When $C_m = 0$, there is just one TZ produced in the high stopband as a result of the harmonic effects. When C_m is greater than 0, a second TZ is produced in the high stopband, and the filter exhibits excellent roll-off in this region.

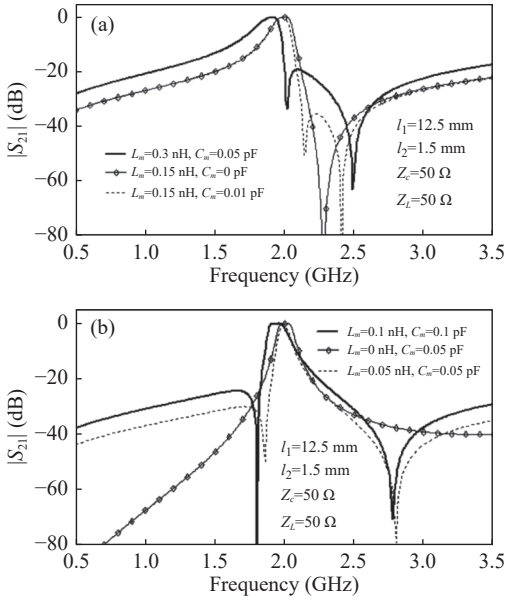

Figure 3 S spectrum responses of SEMCP filters. (a) M dominant; (b) E dominant [1].

Figure 3(b) shows how the coupling elements (L_m and C_m) in the two coupling paths affect filter performance

when the electrical coupling is significant. No finite TZ value may be formed in the stopband when $L_m = 0$. Two more TZs are produced in the stopband when $L_m > 0$, and the filter exhibits a nice roll-off.

To physically implement the SEMCP, we propose three second-order filter structures based on physical path separation (shown in Figure 4). These designs use a modified quarter-wavelength resonator with a coupling gap or coupled transmission line to achieve the lumped capacitance and use either a via-hole or a short section of a high characteristic impedance transmission line grounded through a series-connected via-hole to achieve the lumped inductance.

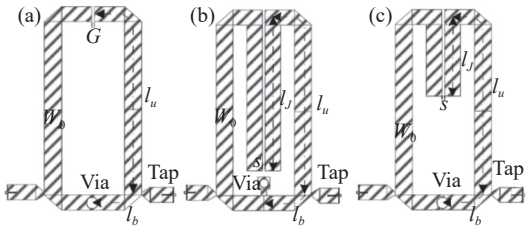

Figure 4 The SEMCP filters. (a) Structure 1; (b) Structure 2; (c) Structure 3 [1].

In such systems, the electric coupling is prominent. The electric and magnetic coupling cancel each other out in the operational frequency range when the external quality factor is known. As a result, the operating frequency falls due to the increasing load on both coupling routes, while the filter bandwidth, which is mostly influenced by the interstage coupling coefficient C, varies minimally. Figure 5(b) illustrates the situation where magnetic coupling dominates. Because of the canceling effect of the two coupling paths, the coupling of each path increases, resulting in a lower operating frequency. As a result, the filter's bandwidth can remain almost unchanged even with increased electrical and magnetic coupling.

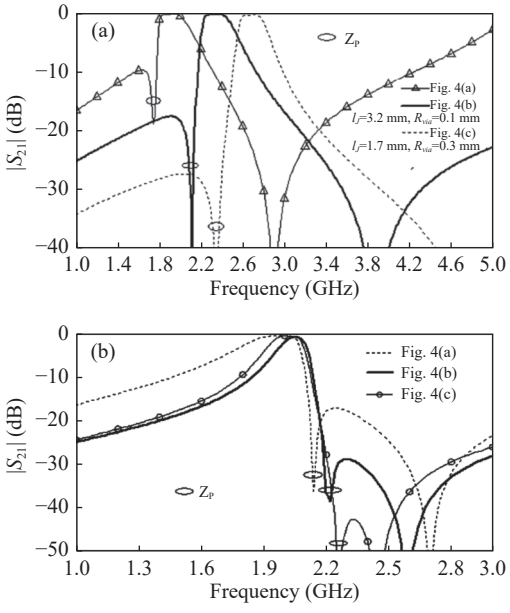

Figure 5 Frequency responses of the SEMCP filters. (a) E dominant; (b) M dominant [1].

Additionally, Figure 6 uses the SEMCP structure to depict the nth-order SEMCP filter topology. Its novelty is that every pair of neighboring resonators in the filter has access to two quasi-independent, controllable E and M coupling paths. Figure 7(a) illustrates how the dominant magnetic coupling can be exploited to generate TZs in the up-

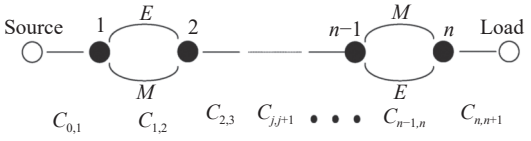

Figure 6 Topology of the high-order SEMCP filter [1].

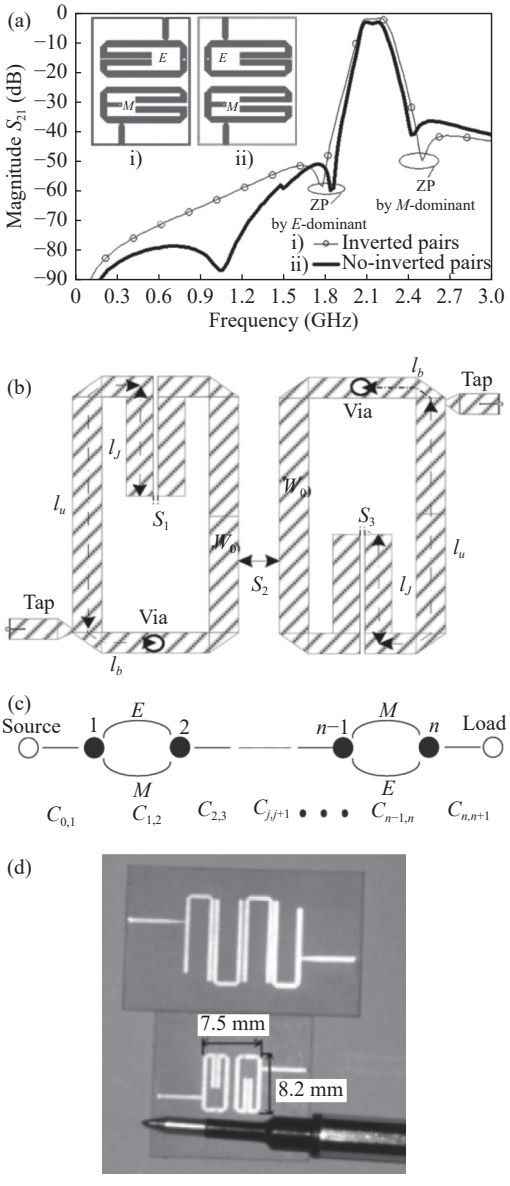

Figure 7 The fourth-order SEMCP filter. (a) Simulation; (b) Configuration; (c) Topology; (d) Comparison photographs with hairpin filter [1].

per reject band while the electric coupling is dominant, and TZs are generated in the lower passband. It is assumed that TZs can be formed in both the upper and lower pass bands if the filter has both the electric and magnetic dominant SEMCPs. Based on this mechanism, the structure and topology of the proposed fourth-order SEMCP filter are shown in Figure 7(b) and Figure 7(c). Compared with the conventional combined filter, each filter generates additional TZs in the upper and lower blocking bands. The introduced TZs of this filter succeed in the minimal insertion loss and small size. Images of the SEMCP filter and the hairpin line filter are shown in Figure 7(d). Just one-third of the constructed hairpin line filter's area is covered by the fourth-order SEMCP filter, which has a surface area of only $0.06\lambda_0 \times 0.0545\lambda_0$. This filter's benefits include controlled TZs in addition to its low insertion loss and compact dimension.

In reference [36], we conducted an additional investigation based on [1] to design a compact filter utilizing a spiral-like resonator with an open ground end (similar to that shown in Figure 8) and explore the mechanism of TZ synthesis based on the equivalent electric and magnetic coupling path separation. The filter topology of the described filter is similar to that of [1]. However, because the structure of a spiral-like resonance is more intricate, the analysis in [1] cannot be used to completely evaluate the proposed filter. If the entire filter is studied using an EM simulator, then the results are merely the combined effect of the electromagnetic coupling channels, without knowledge of the coupling mechanism that underlies them. Because the two paths are parallel and typically only weak electromagnetic coupling occurs between them, it is possible to study the electric coupling path (T path) and the magnetic coupling path (B path) separately and predict the characteristics of the filter response and zeros with some degree of accuracy. Two connected open spirals are used in configuration with the T path, and each spiral can be investigated

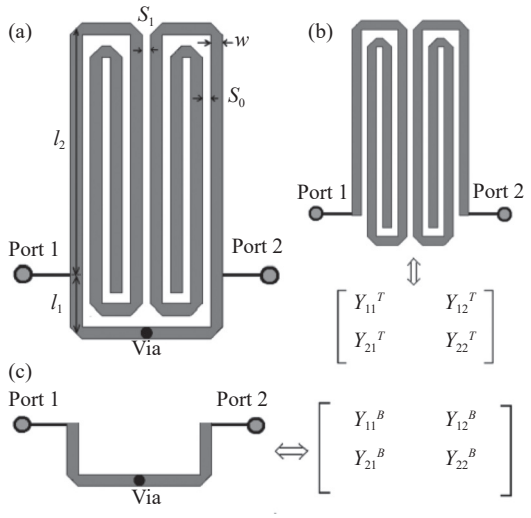

Figure 8 Proposed filter configuration and the equivalent circuits. (a) Configuration; (b) T-path; (c) B-path [36].

independently using the full-wave EM software. The S-matrix for the T-path and B-path can be calculated because the structures are symmetric. Under no-loss or low-loss conditions, the generation of filter zeros in Figure 8(a) should satisfy (6) as

$$\text{imag}\left(Y_{21}\right) = \text{imag}\left(Y_{21}^T + Y_{21}^B\right) = 0 \tag{9}$$

The estimated findings for two different examples (Case 1: S_1=0.15 and Case 2: S_1=0.35) are shown in Figure 9 and Figure 10. 1.5 and 1.64 GHz are the initial transmission points TZ1 determined using equation (6). For both cases, the second transmission point, or TZ2, is almost at the same frequency, approximately 2.03 GHz. The spectral positions of the investigated zeros in Figures 9 and 10 are in excellent agreement.

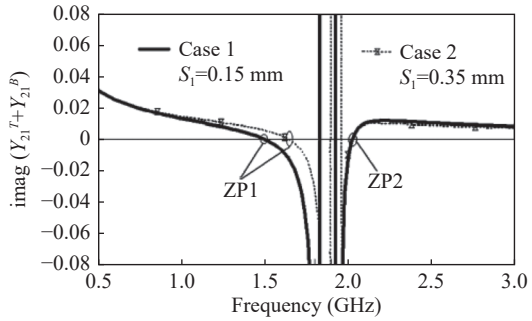

Figure 9 Impedance and zero points (ZPs) of the filter in Figure 8(a) [36].

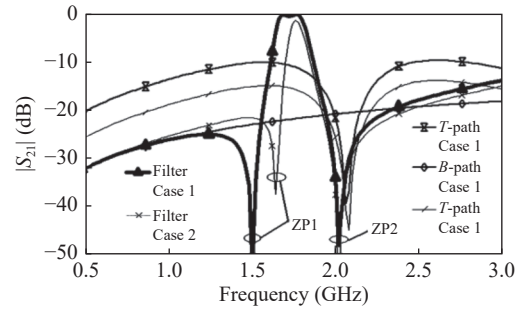

Figure 10 Transmission characteristics of the filter in Figure 8(a) [36].

The fourth-order filter's topology, simulated, and measured results are shown in Figure 11 and Figure 12, respectively. The results demonstrate that the filter has improved selectivity, more TZs, and a smaller size. This hairpin filter has a smaller size ($0.031\lambda_0 \times 0.035\lambda_0$) than the conventional fourth-order hairpin filter ($0.094\lambda_0 \times 0.11\lambda_0$).

Employing the fundamental electric and magnetic coupling block, we could introduce SEMCP in various classical filtering topologies, such as the in-line, CT, or CQ topologies. Exploring the SEMCP between cross-coupled resonators can introduce additional TZs, which is very beneficial for designing high-selectivity bandpass filters. For example, a CT topology with electric and magnetic coupling generated 2 TZs between nonadjacent resonators. Compared with the classical CT topology, which can only

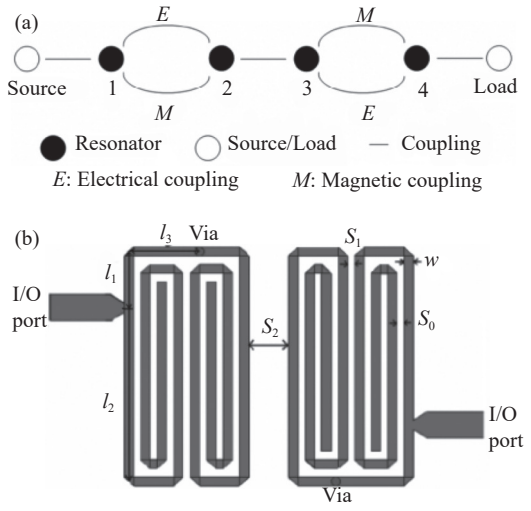

Figure 11 Proposed fourth-order hairpin filter configuration and the topology: (a) filter configuration and (b) filter topology [36].

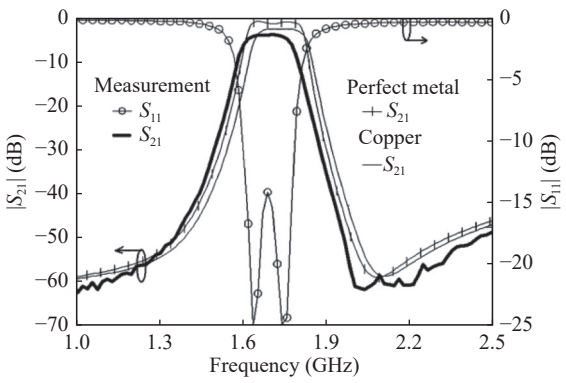

Figure 12 Comparison of measured and simulated results of proposed fourth-order quasihairpin filter [36].

produce one TZ with cross-coupling, the employment of such novel EM couplings can introduce one more TZ, thus achieving high selectivity.

The most popular way to introduce multiple TZs for outband suppression is by utilizing the standard cross-coupling method. Nevertheless, when the number of TZs is beyond half of the passband orders, complex cross-coupling structures will inevitably be introduced in cross-coupled topologies. To explain these advances in electric and magnetic coupling, a six-order BPF with four TZs is considered here. Based on the coupling matrix method, the synthesized topology is shown in Figure 13(a). As we can observe from the topology, cross-couplings exist in resonators 1 and 5 and resonators 2 and 4, which are quite difficult to implement in various technologies. This may also cause problems in filter tuning. The extracted pole topology shown in Figure 13(b) may be an answer to arranging an arbitrary number of TZs with an in-line topology. However, in this topology, each TZ is produced by a dangling resonator, and the dangling resonators refer to resonators 7, 8, 9 and 10 in succession. Thus, the overall sizes are quite large, and it's not so related to the filters' minimization. Nevertheless, the use of SEMCP topology can be a very favorable solution to tackle this issue. Figure 13(c) shows a six-order bandpass filter with four TZs working at the 5.8 GHz WiFi frequency. As we can see, it can be realized with four SEMCP coupling structures without any cumbersome cross-couplings. Figure 14 presents the synthesized results of the proposed in-line bandpass filter. The out-band attenuation is better than −85 dB, which is a satisfying result for nearly all applications in this spectrum range.

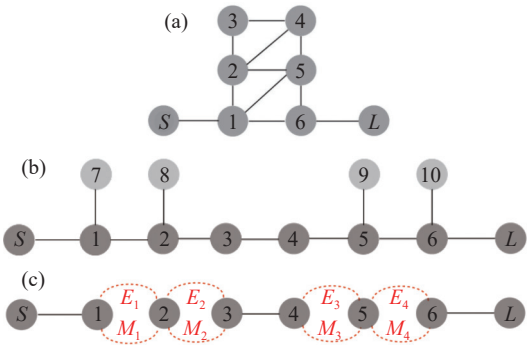

Figure 13 The six-order in-line topology with electric and magnetic coupling. (a) The classical folded topology; (b) The extracted pole topology; (c) The six-order in-line topology with electric and magnetic coupling.

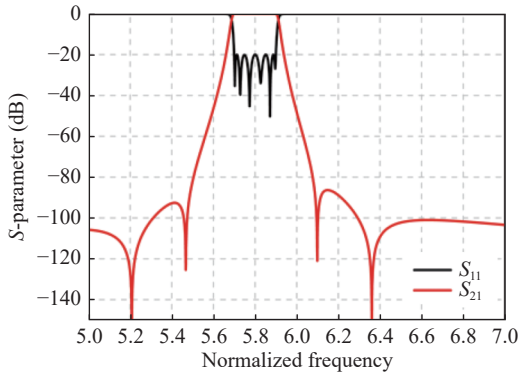

Figure 14 The frequency responses of the six-order filter employing SEMCP at 5.8 GHz for WiFi applications. The in-band return loss is −20 dB with four TZs located at 5.208 GHz, 5.467 GHz, 6.099 GHz, and 6.361 GHz, successively.

More efforts are focusing on this type of approach, and many excellent circuits have been proposed to accomplish it. This increased attention is because the separate electric and magnetic coupling path theory can provide many advantages to filter design by adding more zeros and allowing their control. An open-loop microstrip resonator filter with one or more TZs is suggested in [37]. The term "electric and magnetic mixed coupling" shows the "separating electric and magnetic coupling paths" in electric behavior or the derived equation. The SEMCP is produced in two coupled resonators by combining the coupled sides with the maximum magnetic field and the open gaps with the maximum electric field. In the proposed coupled SEMCP filter, the coupling coefficients may be modified, and adjustable TZs in the lower stopband, higher stopband, or both can be

created by altering the spacing between resonators and the locations of open gaps. The second-order mixed coupled filter with equivalent SEMCP (based on magnetic coupling dominant in the middle of the half-wavelength resonator, while electric coupling is dominant close to the open ends of the half-wavelength resonator), which has a footprint of just $0.13\lambda_0 \times 0.1\lambda_0$ (without accounting for the I/O feed), is shown as a photograph in Figure 15.

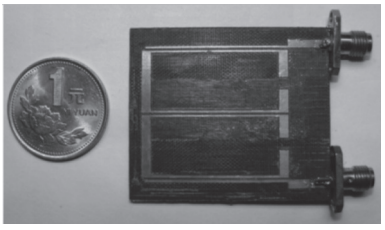

Figure 15 Fabricated second-order microstrip filter [37].

On the basis of reference [37], a new triangular open-loop filter [38] shown in Figure 16 is proposed to realize very close-to-band TZs and a relatively wide passband at the same time. When compared to conventional square loops, these triangular loops exhibit stronger coupling as well as more controllable electric and magnetic coupling ratios. A manufactured three-pole triangular open-loop filter reaches a 6% 3-dB bandwidth while having very tight TZs. The tested performance is better than that described in [37].

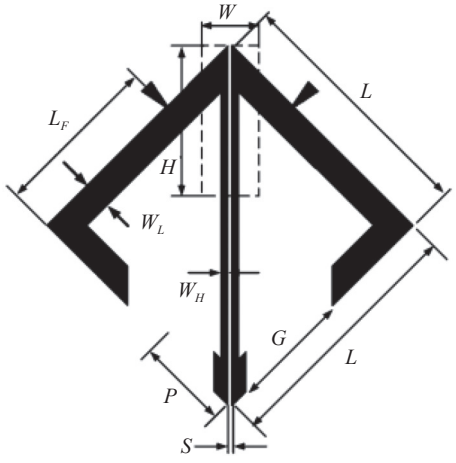

Figure 16 Geometric structure of a two-pole triangular resonator mixed coupled filter with SEMCP backed aperture [38].

The proposed filter in [31] uses a low-loss SISL platform [12] by utilizing a differential inductor—which is frequently used as an inductive element—as a resonator that can operate in the 700-MHz spectrum in the low 5G band. A T-shaped coupling structure (as shown in Figure 17) is first proposed on SISL to improve the stopband selectivity, and the ideal position of TZs is attained by reducing the electrical coupling and improving the magnetic coupling. Edge coupling is used to achieve magnetic dominant coupling based on the physical path separation theory. A narrower gap g_s and thinner W_s can improve the coupling. Without using any extra techniques to enlarge the stopband, the second-order mode is 5.7/3.92 times the operating band. Second-order and fourth-order BPFs' 20-dB roll-off rates fell by 58.8% and 66.1%, respectively.

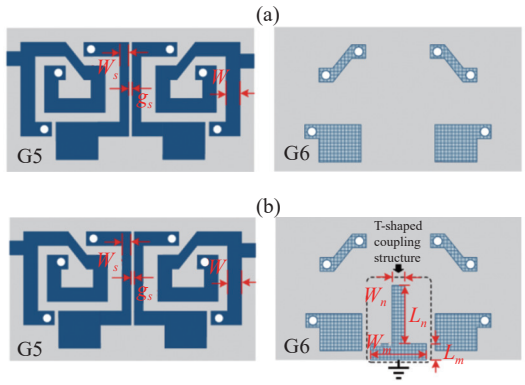

Figure 17 Layout of a second-order filter with magnetic dominant coupling. (a) Without a T-shaped structure; (b) With a T-shaped structure [31].

Physical path separation is also applicable in circuit design of dual-pass band filters to achieve the introduction and independent control of TZs. In [39], the authors present a dual bandpass filter (DBBPF) based on the SISL platform. To increase skirt selectivity, additional TZs are created utilizing SEMCP between two different filter bands. The suggested filters implement various electric and magnetic coupling strategies for dual-band, small-size, and multiple TZs using a hybrid spiral structure. Figure 18 illustrates a novel topology that is proposed in [39]. In addition to synchronously tuned resonators, SEMCP also exists between asynchronous resonators. In the proposed second-order DBBFP, three zeros were introduced by SEMCP.

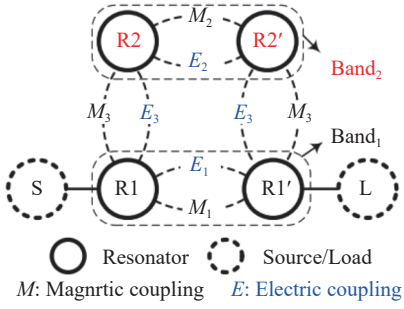

Figure 18 The topology structure of the proposed DBBPF [39].

A short-stub-loaded resistor (SSLR) and two modified feed lines make up another DBBPF [40]. In Figure 19(a), the SSLR can generate the first passband with odd-mode and even-mode analysis of the modes shown in Figure 19(b) and Figure 19(c), respectively. The short-stub-loaded line can be characterized by the inductance L_m, i.e., of the magnetic coupling path, while the coupling gap can be characterized by the capacitance C_m, i.e., of the electrical coupling path. The suggested SSLR is a magnetically coupled dominant filter because of its weak electrical coupling but strong magnetic coupling. The dual-passband filter is

implemented in [41] and [42] by using a similar method of physical path separation. The structure of the main coupling pattern of the stepped-impedance resonator (SIR) in [41] and the topology are shown in Figure 20. This filter introduces multiple zeros by using a combination of physical path separation and source-load coupling.

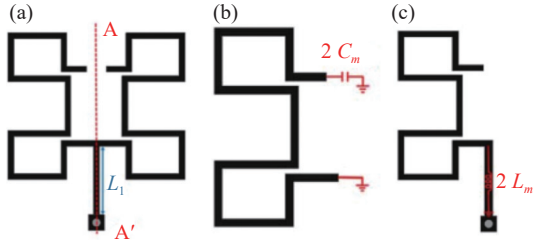

Figure 19 (a) SSLR; (b) Odd mode; (c) Even mode [40].

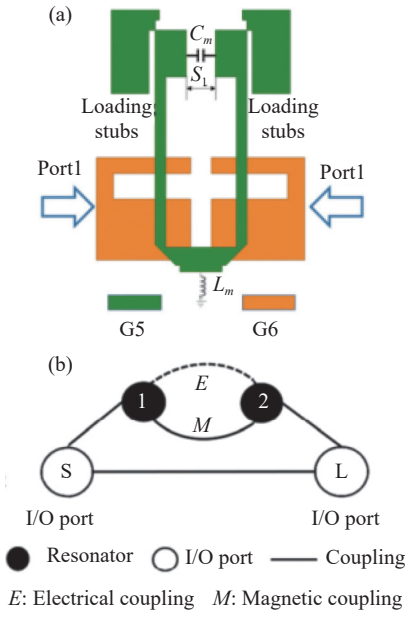

Figure 20 (a) Main coupling pattern of SIR-I; (b) Topology of SIR-I [41].

A filter that separates electric and magnetic coupling routes on a multilayer structure on low-temperature cofired ceramic (LTCC) is proposed in reference [43] and is based on physical path separation methods. The suggested resonator is illustrated in Figure 21(a) and is composed of two independent parallel coupling channels, one for electrical coupling (*E*-path), as shown in Figure 21(b), and the other for magnetic coupling (*M*-path), as shown in Figure 21(c), both of which are constructed on three metallic layers. As a common ground plane, layer 2 physically separates the *E*-path and *M*-path so that these two paths can be controlled separately.

In addition to the planar circuit, the authors in [44] also an inline coaxial filter that introduces the separating electric and magnetic coupling paths to achieve independent control of the TZs. As shown in Figure 22, the metal cap at the open end of the inner rod is equivalent to a load capacitor that acts as an electrical coupling path between

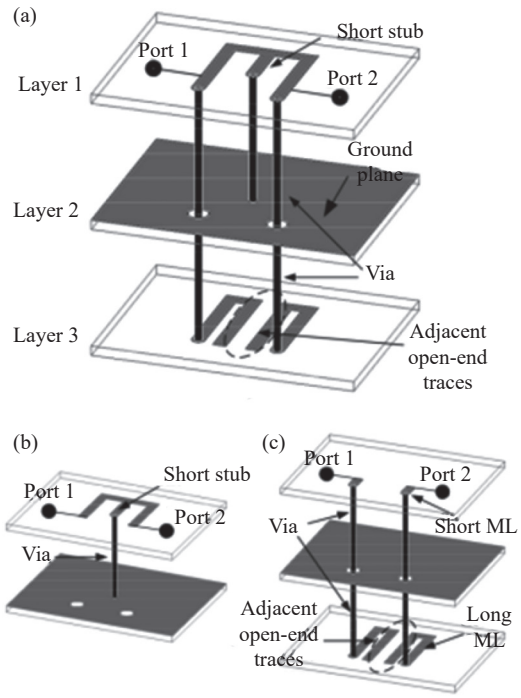

Figure 21 Proposed second-order filter configuration and equivalent circuits. (a) Proposed filter; (b) *M*-path; and (c) *E*-path [43].

the two cavities. To further enhance the electrical coupling strength, a conductive strip attached to the dielectric substrate is inserted in the coupling iris and connects the caps of the two inner rods. In addition, the equivalent magnetic coupling path is achieved by the current of the conductive pin, tapping the abdomen of the two adjacent rods. As shown in Figure 23, controllable TZs are also achieved in the coaxial waveguide cavity filter by introducing SEMCP in [45].

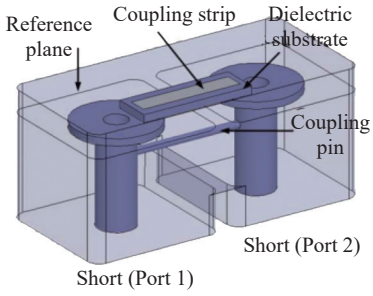

Figure 22 Proposed second-order coaxial cavities filter configuration [44].

In [46], a wide stopband filter combining the separating electric and magnetic coupling paths with CT coupling was also proposed, as shown in Figure 24. Three quarter-wavelength resonators make up the CT unit. The introduction of controllable electric and magnetic coupling increases the design flexibility. Both the magnetic and electric couplings can be tuned independently. The source-load coupling and inductive cross-coupling result in three TZs. A coupled-line input/output arrangement is used to suppress the third and fifth harmonics and widen the stopband.

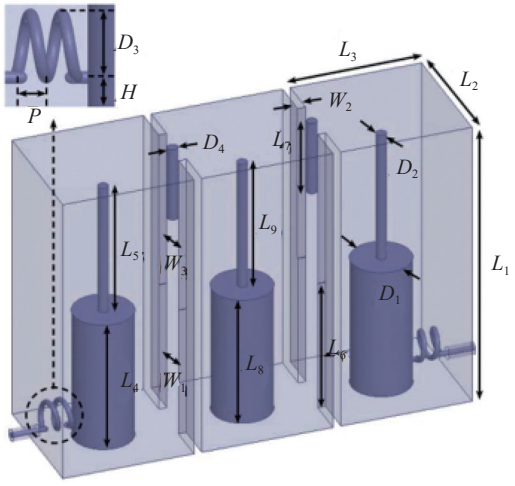

Figure 23 Proposed dual-band coaxial cavity BPF [45].

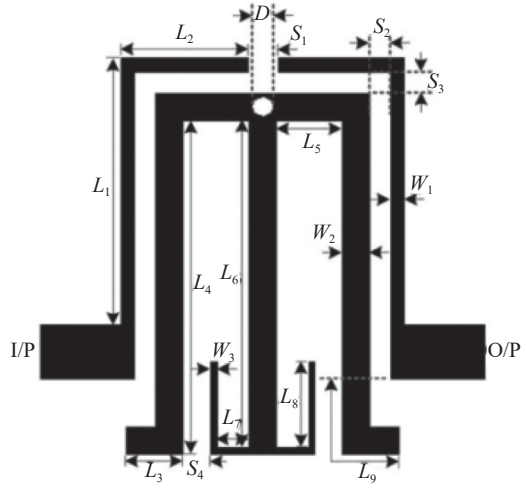

Figure 24 Layout of the CT filter with the separating electric and magnetic coupling paths [46].

Using a two-layer PCB technique, a substrate integrated waveguide (SIW) quasielliptic filter [47] with tunable electric and magnetic coupling was proposed. This SEMCP topology is created by combining an embedded short-ended strip line with a typical inductive window between two cavities. Two SIW cavity resonators with separated electric and magnetic coupling paths are depicted in Figure 25.

The simulated *S*-parameters of the second-order filter are shown in Figure 26. According to Figures 26(a) and (b), magnetic coupling $M_c > E_c$ (electric coupling) results in a TZ in the lower stopband, and $M_c < E_c$ results in a TZ in the upper stopband. Both examples clearly show that the width of the inductive window has a significant impact on the magnetic coupling, while the width of the inserted conducting strip has a significant impact on the electric coupling.

In [48], the design of SIW combine resonator filters with advanced performance was investigated. Various coupling configurations involving magnetic and electric coupling processes have been proposed and thoroughly investigated for this purpose. It has been shown that the suggested

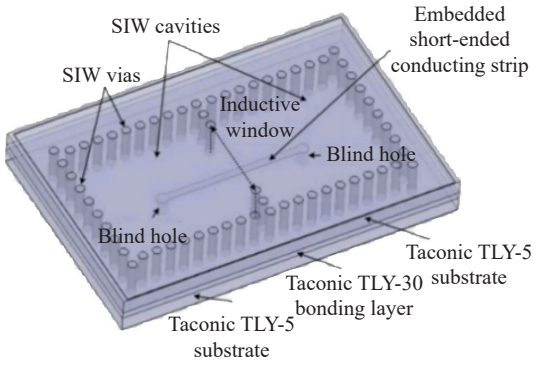

Figure 25 Configuration of two electrically and magnetically mixed coupled SIW cavity resonators [47].

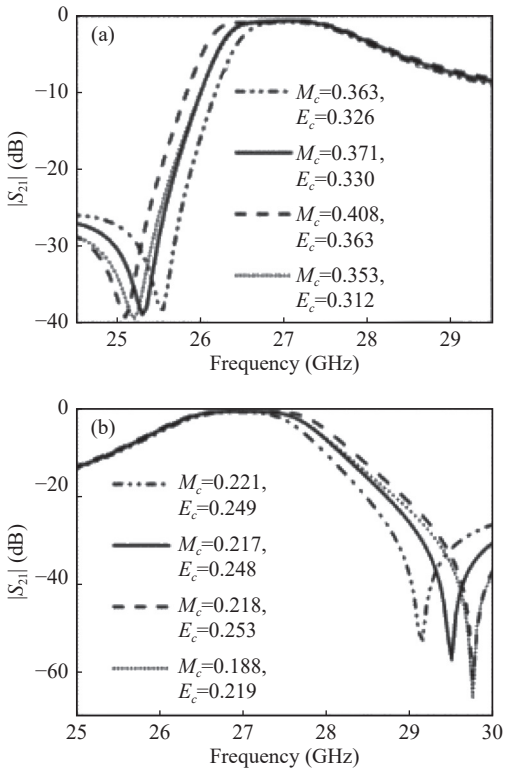

Figure 26 Simulated *S*-parameters of the second-order filter. (a) Magnetic coupling is dominant; (b) Electric coupling is dominant [47].

electric coupling configuration offers a great degree of design flexibility. A filter that presents a highly selective response with a broad rejection band has also been proposed, one that arranges the magnetic and electric coupling methods of SEMCP topology to create a very compact quasielliptic narrowband bandpass filter. Figure 27(a) shows the top view of the coaxial SIW resonator, including its main design parameters. Figure 27(b) shows the variation in the total coupling coefficient $k_{i,i+1}$ as W increases.

The technology of electric and magnetic couplings is used to efficiently create a six-order bandpass SIW filter in [49]. The slots on the top metal plane of a SIW cavity can be appropriately etched to create the cascaded resonators of the filter. Electric coupling is produced by the slots. Ac-

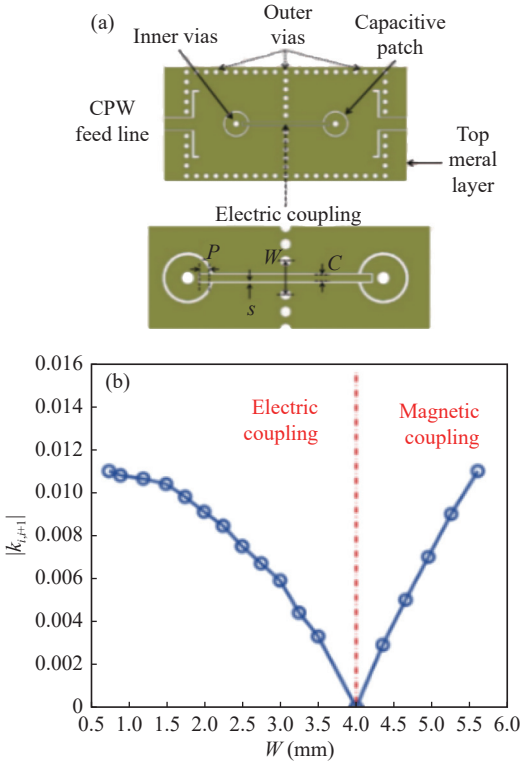

Figure 27 The coaxial SIW resonator. (a) Top view; (b) Coupling coefficient $k_{i,i+1}$ variation versus iris width W [48].

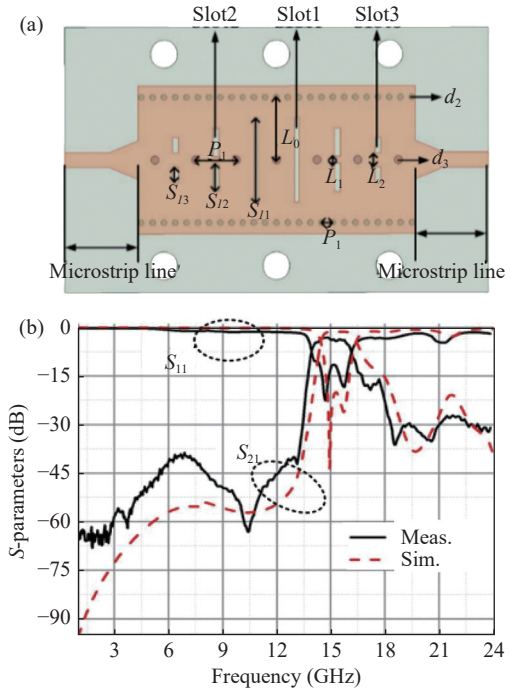

Figure 28 The SIW filter combines electric and magnetic coupling. (a) The view of the upper plane; (b) The measured and simulated *S*-parameters in 1–24 GHz [49].

cording to Figure 28(a), periodic metallic vias in the center of an SIW cavity create magnetic coupling. Two TZ points are reached via the magnetic and electric couplings. Electric coupling influences the upper TZs, and magnetic coupling influences the lower TZs. The measured results are in favorable agreement with the simulated results, as shown in Figure 28(b).

In addition, for optimizing the coupling matrix in the equivalent SEMCP, reference [50] proposed a new technique for synthesizing coupled resonator filters. By using the coupling matrix's eigenvalues of matrix pencils as well as the reference zeros and poles of the scattering parameters to solve a nonlinear least squares problem, it is possible to determine the values of the coupling matrix's nonzero elements. The proposed method with SEMCP topology was confirmed by numerical testing for a variety of coupling schemes, including triplets and quadruplets, for which it was discovered that the frequency-dependent coupling produced an extra zero.

The low-pass prototype can also be transformed in numerous ways to realize synthesis of a circuit with the desired properties. To address the mutual coupling and mutual capacitance of frequency-variant four-states, in [51], the authors suggested a highly selective online topological filter with adjacent frequency-variant couplings (FVCs). Their suggested quadruplet is effectively reduced to an in-line network by involving two matrix rotations and a rescaling operation after particular relations between the variables are met. The changes required can also be expressed by a matrix, which considerably decreases the total number of matrix operations and the associated rounding errors because all of their variables are related to the initial coupling values. The realization of in-line topology filters that contain FVCs inside is shown in Figure 29.

III. Regulation and Control of Electromagnetic Energy Storage in Coupling

1. Fundamentals and circuit-level realization

Considering energy storage applications, the capacitor forms an electric energy storage device, while the inductor presents a magnetic energy storage device. These elements represent an interesting concept of using EM coupling for energy storage. There are three types of EM coupling energy regulation and control (R&C) for RF circuits and systems, namely, electrical coupling R&C, magnetic coupling R&C, and mixed-EM coupling R&C.

For coupled resonators or coupled tanks, all fields, in-

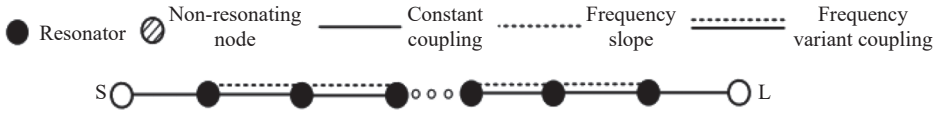

Figure 29 Proposed in-line prototypes [51].

cluding the self-electric field $\overline{E_1}/\overline{E_2}$, magnetic field $\overline{H_1}/\overline{H_2}$, mutual electric coupling $\overline{E_1}\cdot\overline{E_2}$ and mutual magnetic coupling $\overline{H_1}\cdot\overline{H_2}$, are given in Figure 30.

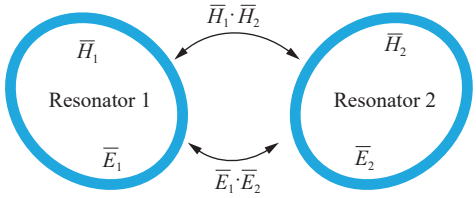

Figure 30 General coupled RF/microwave resonators.

Although resonators with different structures have different self-resonant frequencies, the coupling coefficient k of coupled resonators or tanks can be obtained by definition from the ratio of coupled energy to stored energy as follows [35]:

$$k=\frac{\iiint \varepsilon\overline{E}_1\cdot\overline{E}_2\mathrm{d}v}{\sqrt{\iiint \varepsilon\left|\overline{E}_1\right|^2\mathrm{d}v\times\iiint \varepsilon\left|\overline{E}_2\right|^2\mathrm{d}v}}+\frac{\iiint \mu\overline{H}_1\cdot\overline{H}_2\mathrm{d}v}{\sqrt{\iiint \mu\left|\overline{H}_1\right|^2\mathrm{d}v\times\iiint \mu\left|\overline{H}_2\right|^2\mathrm{d}v}} \tag{10}$$

where ε and μ denote the permittivity and permeability, respectively. The coupling coefficient k comprises electric coupling and magnetic coupling, corresponding to the first term and second term, respectively. According to (7), the stored energy can be mathematically described by the dot operation of field vectors $\overline{E}$ and $\overline{H}$, which results in either positive-sign coupling or negative-sign coupling. The stored energy of uncoupled resonators is enhanced if the polarity is positive, and vice versa. Obviously, the electric and magnetic couplings could result in the same or opposite effects based on the polarity of dot operations.

At RF frequencies, EM energy is usually stored, transferred, and modulated using certain types of resonators in circuits and systems. These resonators are in the form of transmission-line resonators, coaxial resonators, dielectric resonators, crystal resonators, surface acoustic wave resonators, mixed-mode resonators, etc. In general, the simplest resonator is realized by parallel or series inductors and capacitors, a.k.a. LC-tanks, which are often used to model other forms of resonators.

Because N coupled resonators in a magnetic field can be equivalent to N coupled LC-tanks in a magnetic field, as shown in Figure 31, all inductors are generally coupled to each other, which can be treated as an N-coil magnetic coupled transformer [2]. To facilitate the analysis, it is assumed that all LC tanks are identical with self-inductances of $L_1=L_2=L_3=\cdots=L_N=L/N$ and self-capacitances of $C_1=C_2=C_3=\cdots=C_N=C$, and the magnetic coupling coefficient between any two tanks is k [5]. Then, the resonant frequencies of N coupled LC tanks can be expressed as

$$\omega_1=\sqrt{\frac{N}{LC[1+(N-1)k]}} \tag{11}$$

$$\omega_2=\sqrt{\frac{N}{LC(1-k)}} \tag{12}$$

where ω_1 and ω_2 are two different resonant frequencies. Generally, the lower frequency ω_1 is selected as the main resonating frequency. Assuming $k=1$, ω_1 and ω_2 are calculated as $(LC)^{-1/2}$ and approaching infinity, respectively. The effective Q-factor at ω_1 is expressed as

$$Q_{\text{eff}}=\left(\frac{N^3+1.5N\dfrac{CR^2}{L}+0.5\left(\dfrac{CR^2}{L}\right)^2}{N^3+N(1+N)\dfrac{CR^2}{L}+\left(\dfrac{CR^2}{L}\right)^2}\right)\frac{N\omega L}{R} \tag{13}$$

where R is the resistance of the tank. Typically, R^2C/L is much smaller than 1, which leads to a deducted Q_{eff} as

$$Q_{\text{eff}}\approx\frac{N\omega L}{R} \tag{14}$$

Thus, the effective Q-factor of the N-coupled tank is N times higher than that of a single LC tank. The system thus becomes a favorable EM-energy storage and transferring method in the RF and millimeter-wave (mm-wave) frequencies.

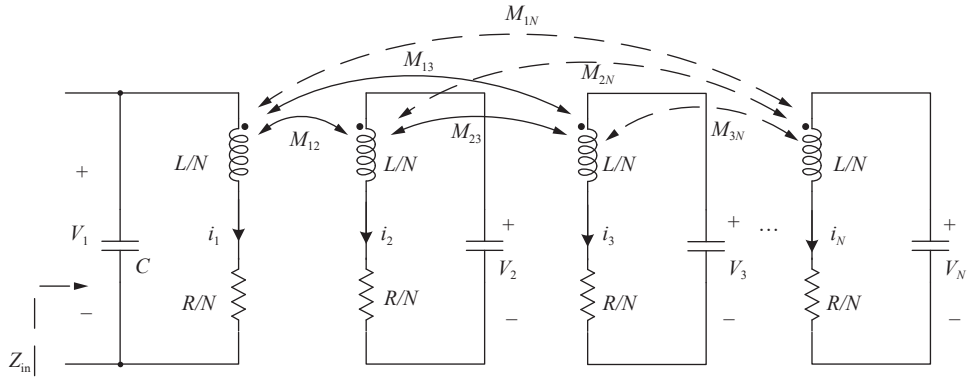

Figure 31 The circuit schematic and equivalent circuit of multiple tanks topology.

2. Regulation and control based on multiple tanks

With the development of wireless communication, radio frequency integrated circuits (RFICs) and mm-wave ICs have attracted widespread attention. As the frequency increases, high substrate loss and metal loss of commercial silicon will lead to performance degradation of the circuit and is not conducive to the design of some structures. The current silicon-based process generally has thick metal layers with low resistivity on the top layer, which can be used to make spiral inductors. However, how to maintain a favorable Q-factor for small inductance devices, especially at high frequency, is a challenging problem worth studying. This problem can be effectively solved by improving the quality factor of the resonators through multiple coupled *LC* resonators [2].

Multitank technology has great application value, such as linear and nonlinear circuits, systems, transceiver modules, multiport systems, low loss matching, high power combination, and off-chip applications. The following is the specific application.

1) Multitank-based linear circuits (Switch and PA)

In RF/mm-wave circuits and systems, linear circuits, such as switches and power amplifiers (PAs), could impact the overall system performance, and low insertion loss of passive networks is a key requirement in linear circuits. Due to the enhanced Q-factor, multiple tanks [2] are adopted in linear circuits of mm-wave switches [3] and reconfigurable amplifiers [4].

In reference [6], a PA with a 4-way power combiner is proposed based on multiple coupled LC tanks, as shown in Figure 32. Using multiple coupled LC tanks, the power combiner achieves a compact size and high efficiency of PA. Fabricated in GF's standard 65 nm CMOS process, the 3 dB bandwidth is 16 GHz, the in-band power gain is greater than 23.8 dB, and the saturated output power is 19.7 dBm. The peak power-added efficiency (PAE) at 60 GHz is 13.4% with a chip area of 0.32 mm^2. Compared with the previous design [52], the size of the power synthesizer is less than one quarter.

Switches are also an indispensable component of linear circuits. In reference [7], a single-pole double-throw (SPDT) switch using a magically switchable artificial resonator structure, which can be modeled as triple-coupled LC tanks, could effectively alleviate the problem of $\lambda_g/4$ transmission line area, as exhibited in Figure 33. The SPDT switch is manufactured by a 65 nm CMOS process with a core area of only 0.0035 mm^2. The measured insertion loss of the switch is 3.3 dB at 155 GHz and is less than 4 dB from 140 to 180 GHz. The isolation in the range of 140 to 180 GHz is greater than 21.8 dB, and the return losses from 130 to 180 GHz exceed 10 dB. Compared to typical SPDT topologies [53], the circuit size is reduced by 96.5%.

2) Multitank-based nonlinear circuits (VCO, ILFD, frequency multiplier)

The oscillation frequency of the voltage-controlled oscillator (VCO) is tunable by adjusting the energy stored in the capacitor. In reference [54], a K-band differential Colpitts VCO using a 0.18-μm SiGe BiCMOS process was demonstrated, as shown in Figure 34. This design forms a tri-coupled LC tank via varactor diodes, capacitor banks, and strongly tri-coupled inductors. Without sacrificing

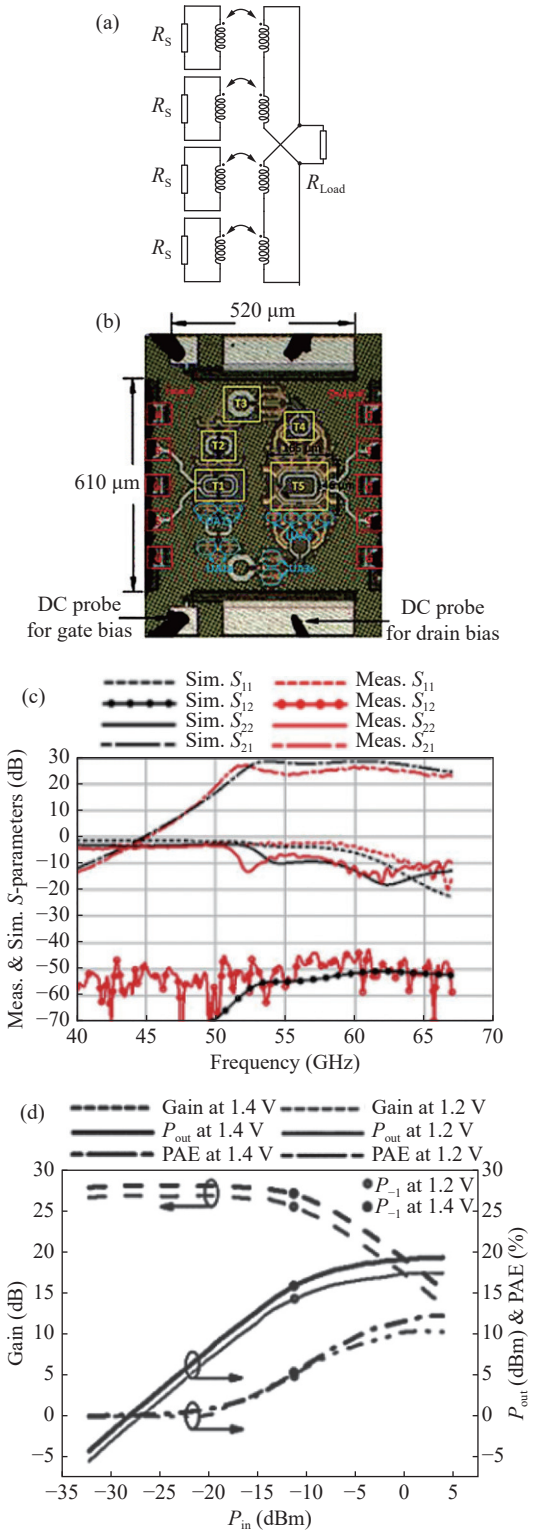

Figure 32 The PA with 4-way hybrid coupling combiner. (a) 4-way combiner configurations; (b) Chip micrograph; (c) Measured and simulated *S*-parameters; (d) Measured power result at 60 GHz [6].

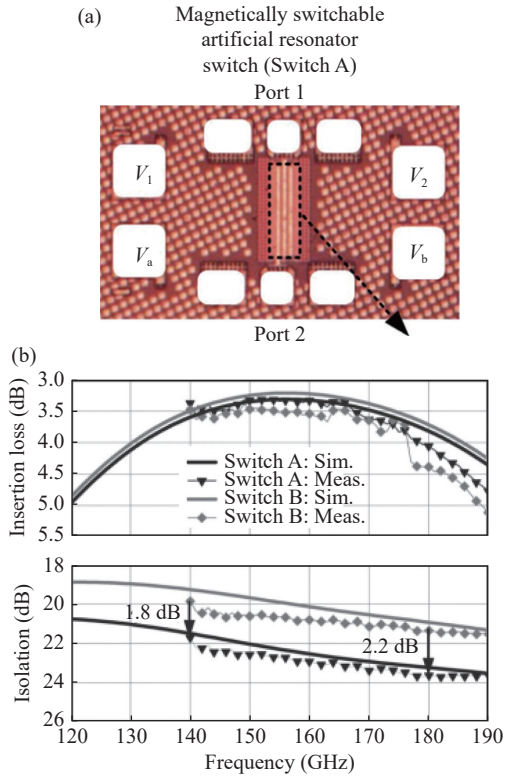

Figure 33 The coupling-switchable SPDT switch. (a) Chip micrograph; (b) Insertion loss and isolation performance of the SPDT switches [7].

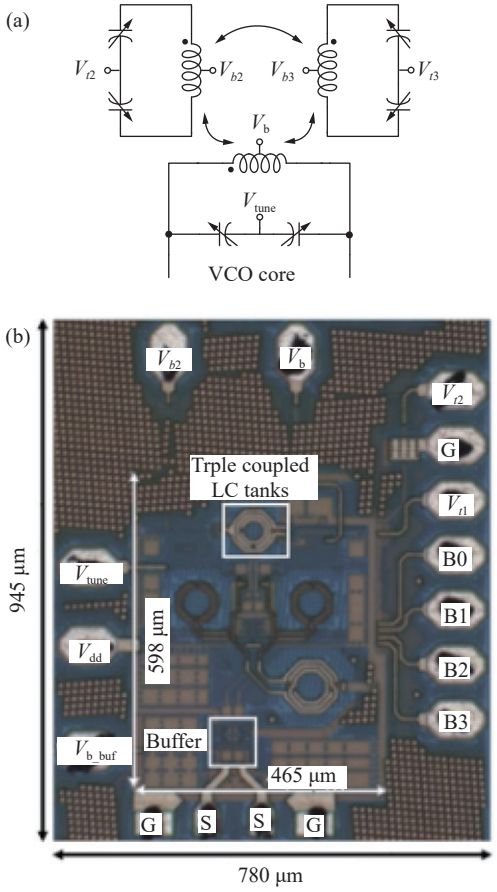

Figure 34 Triple-coupled LC tanks based VCO. (a) Schematic of the triple-coupled LC tanks; (b) Chip micrograph [54].

phase noise, it increases the tuning range of the VCO. The measured frequency tuning range is 22.5 to 26.23 GHz (15.3%). The phase noise of the VCO at 1 MHz and 10 MHz is –107.7 dBc/Hz and –132 dBc/Hz, respectively. It has an output power of –3.1 dBm at 24 GHz. The oscillator core and buffer consume 8.2 and 5.4 mW, respectively, under a 1.8 V power supply voltage.

In reference [55], a switched-core VCO was reported, as shown in Figure 35. The oscillator has a switchable VCO core to enhance the frequency tuning range. The inductors of the two VCO cores are strongly coupled with the inductors of the frequency multiplier, and the required signals are output to the frequency multiplier. By controlling the microcurrent source, Core-1 and Core-2 become switchable. Fabricated in 0.18-μm SiGe technology, the measured frequency tuning range is 17% with phase noise of –93.45 dBc/Hz and –89.4 dBc/Hz at a 1-MHz offset in two operating modes. The power consumed by the oscillator ranges from 7.6 to 15.5 mW.

Figure 36 shows an injection locked frequency divider (ILFD) with dual *LC*-tanks for bandwidth extension [8]. The ILFD adopts the 0.18 μm SiGe BiCMOS process. The transformer is made of top metal with an area of 123×123 μm^2. The circuit consumes 4.8 mW DC power under a 1.8 V power supply, and the buffer is 3.8 mW. The divider locks from 20.09 to 25.86 GHz under 0 dBm input. The maximum output power is 3.23 dBm, and the measured phase noise is −116.07 dBc/Hz@10 kHz at 25 GHz.

Figure 37 shows a reconfigurable injection locked frequency multiplier (RE-ILFM) [9]. Simultaneous ×2 and ×3 modes are realized with common input and output ports. In addition, multiple tanks are introduced into the ILFM for the first time to effectively improve the amplitude of the output signal and reduce the circuit area. The design accelerates the roll-off of the output signal amplitude in the ×3 mode and forms an isolation band at the edge of the locked frequency. When the differential injection power is 0 dBm, the bandwidth of RE-ILFM is from 20.7 to 43.8 GHz, the frequency tuning range (FTR) is 71.6%, and the harmonic rejection is better than 27 dB. The circuit is designed by a 55-nm CMOS process with a core area of 0.07 mm^2.

3) Multitumors for the frequency synthesizer and transceiver

Figure 38 shows a 270 GHz injection locked frequency synthesizer [10]. A sub terahertz (sub-THz) mixer is used for frequency expansion by a subsampling phase-locked loop (SS-PLL) and a mm-wave ILFM. The linearity of the structure is improved by distributed bias technology. VCO, ILFM and other structures in the system use multiple tanks to improve performance. The system is designed with a 65-nm CMOS process. The core area of the chip is 0.58 mm^2. It can achieve ultrawide frequency tuning ranges of 61.2 to 100.8, 122.4 to 136.8, and 198.5 to 273.6 GHz with −79.3 to −95.4 dBc/Hz phase noise at a 1-MHz offset. An inte-

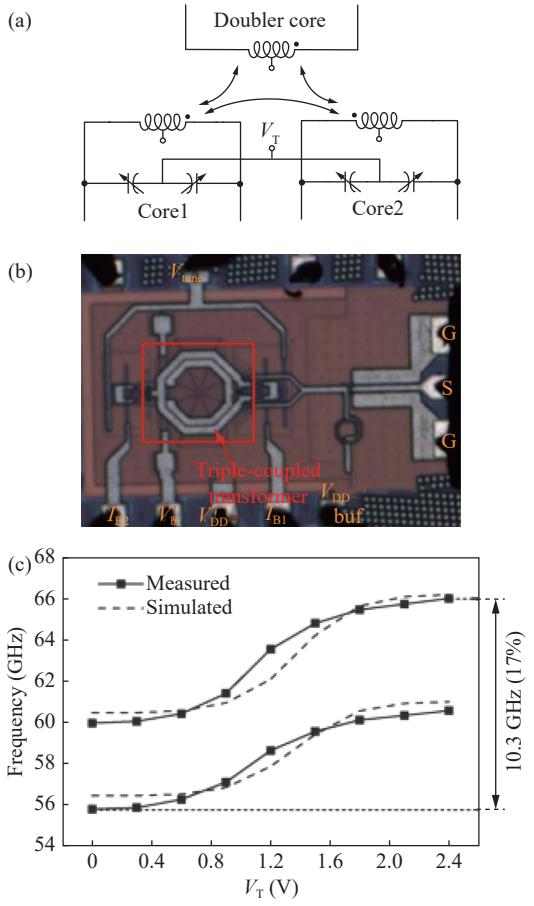

Figure 35 Poposed VCO. (a) Schematic of proposed VCO with switchable coupled VCO-cores; (b) Chip micrograph; (c) Measured oscillation frequency [55].

gral jitter of 124 to 159 fs is observed in the tuning range. The measured output power is −11 dBm at 211.4 GHz, and

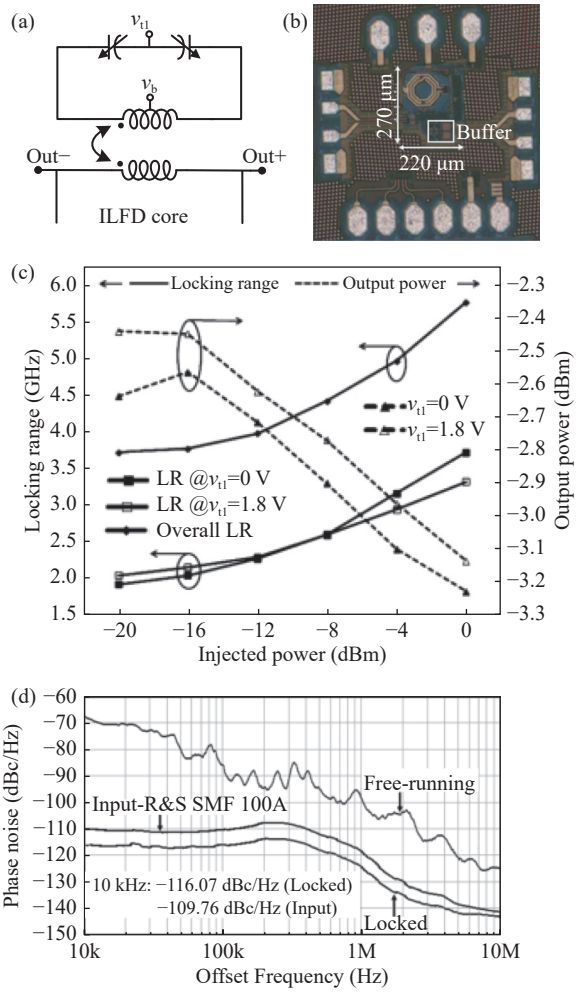

Figure 36 Proposed dual tanks-based ILFD. (a) Topology of injection locked divide-by-2 divider; (b) Chip micrograph; (c) Measured locking range and output power; (d) Measured ILFD phase noise [8].

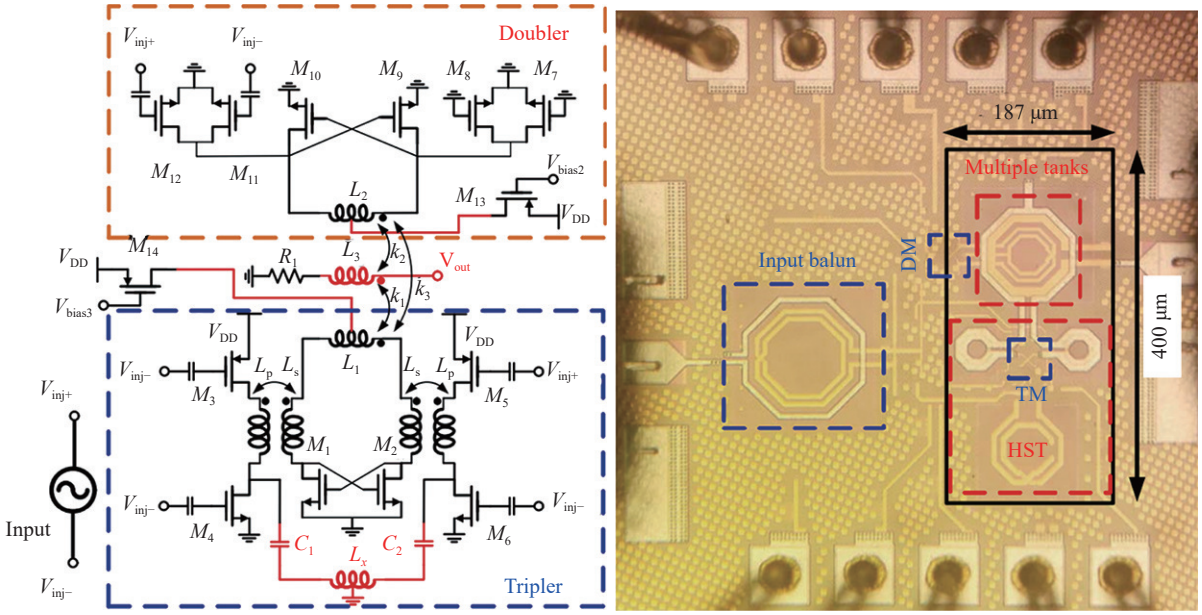

Figure 37 Reconfigurable injection locked frequency multiplier [9].

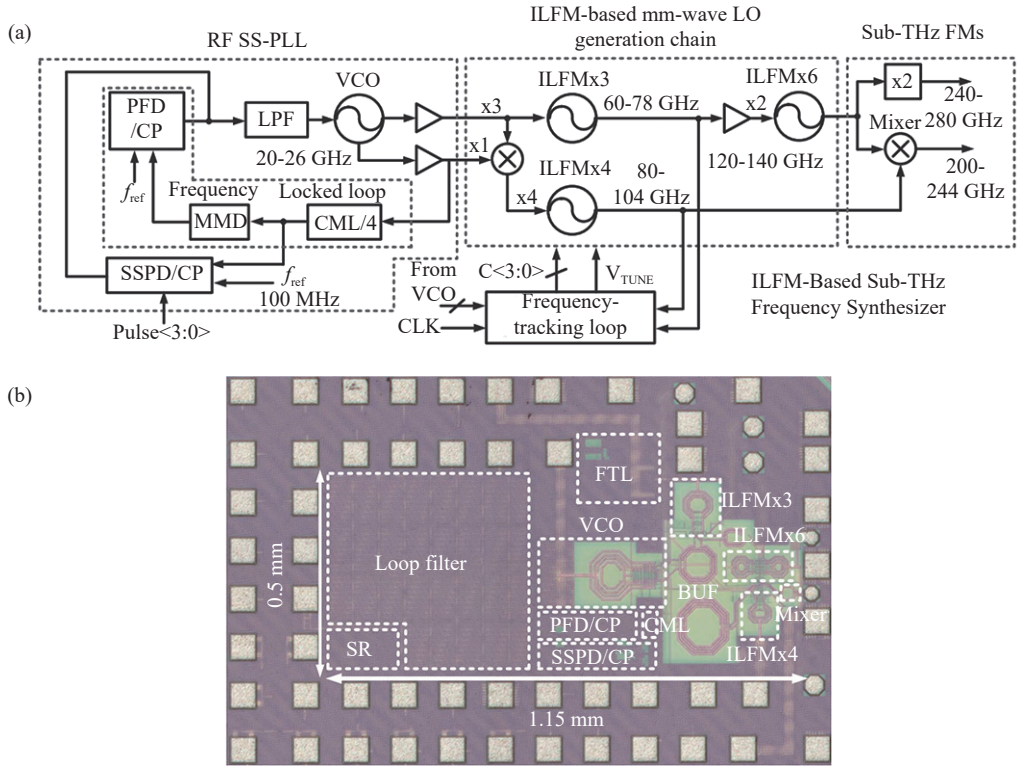

Figure 38 Proposed frequency synthesizer. (a) Block diagram and frequency plan of the sub-THz frequency synthesizer; (b) Chip micrograph [10].

the corresponding consumption is 49.5 mW. The DC-RF efficiency of the system is 0.16%.

In reference [11], a 60 GHz low-power wireless communication system based on the IEEE 802.11ad standard, comprising a baseband integrated circuit (BBIC) and a low-power 60 GHz RFIC adopting multitank techniques, was proposed, as shown in Figure 39. An adaptive time-domain equalizer (TDE) is adopted in the BBIC system, which not only reduces power consumption but also allows a smaller hardware size of the equalization process than the frequency domain equalizer (FDE). The BBIC uses a 16-bit parallel host interface to support the max throughput of 4.6 Gbps. A 6-bit DAC/ADC in the BBIC connects the input/output differential "I" and "Q" analogy signals of the RFIC. The 60 GHz RFIC comprises a Tx chain, a synthesizer with a local oscillator (LO) network, SPI slave, and an Rx chain. Through the LO feed network, the 22.5–26.23 GHz synthesizer with a K-band multitank VCO, an ILFD and a PLL can be shared as the LO. In the Tx/Rx chain, four sets of cross-coupled (CC) low-pass filters (LPFs) filter the differential I/Q analogy signals from/to the BBIC. The Rx chain includes a 60 GHz low noise amplifier (LNA), a 60 GHz downconversion subharmonic mixer (SHM), which converts the differential signals to intermediate frequency (IF), IF variable gain amplifiers (IF VGA), and a digitally variable gain amplifier (DVGA). This dual-chip system delivers 9.8% error vector magnitude (EVM) for 16QAM with a symbol rate of 1 GHz.

IV. Dielectric, Air and Substrate Electromagnetic Regulation Technique and Circuits

1. Quasiplanar circuits with embedded air cavities

There are many explanations for the loss of electromagnetic waves in space and the substrate, mainly dielectric loss, conductor loss and radiation loss. In the traditional planar circuits [56], such as microstrips, coplanar waveguides (CPWs), and striplines, the EM field is partially or wholly located in the substrate, which will cause large dielectric loss. Generally, the transmission loss in air is much smaller than that in a lossy substrate. In view of these dynamics, if the lossy substrate in planar circuits can be replaced by air, there would be almost no dielectric loss in the ideal situation.

In recent years, the quasiplanar structure with embedded air cavities proposed in reference [12] has been widely investigated and named SISL. Further development of the SISL platform [13], air-filled SIW [14], and empty substrate integrated waveguide (ESIW) [15] all include this air-embedded concept. Among them, the SISL platform is a typical representative of using air cavities. In SISL, the electromagnetic field is mainly located in the air, which significantly reduces dielectric loss.

Figure 40 shows the difference in electromagnetic field distribution between SISL and microstrip lines [16]. SISL also has other characteristics, such as low cost, high integration level, and self-packaging.

With the advantage of the low dielectric loss of the

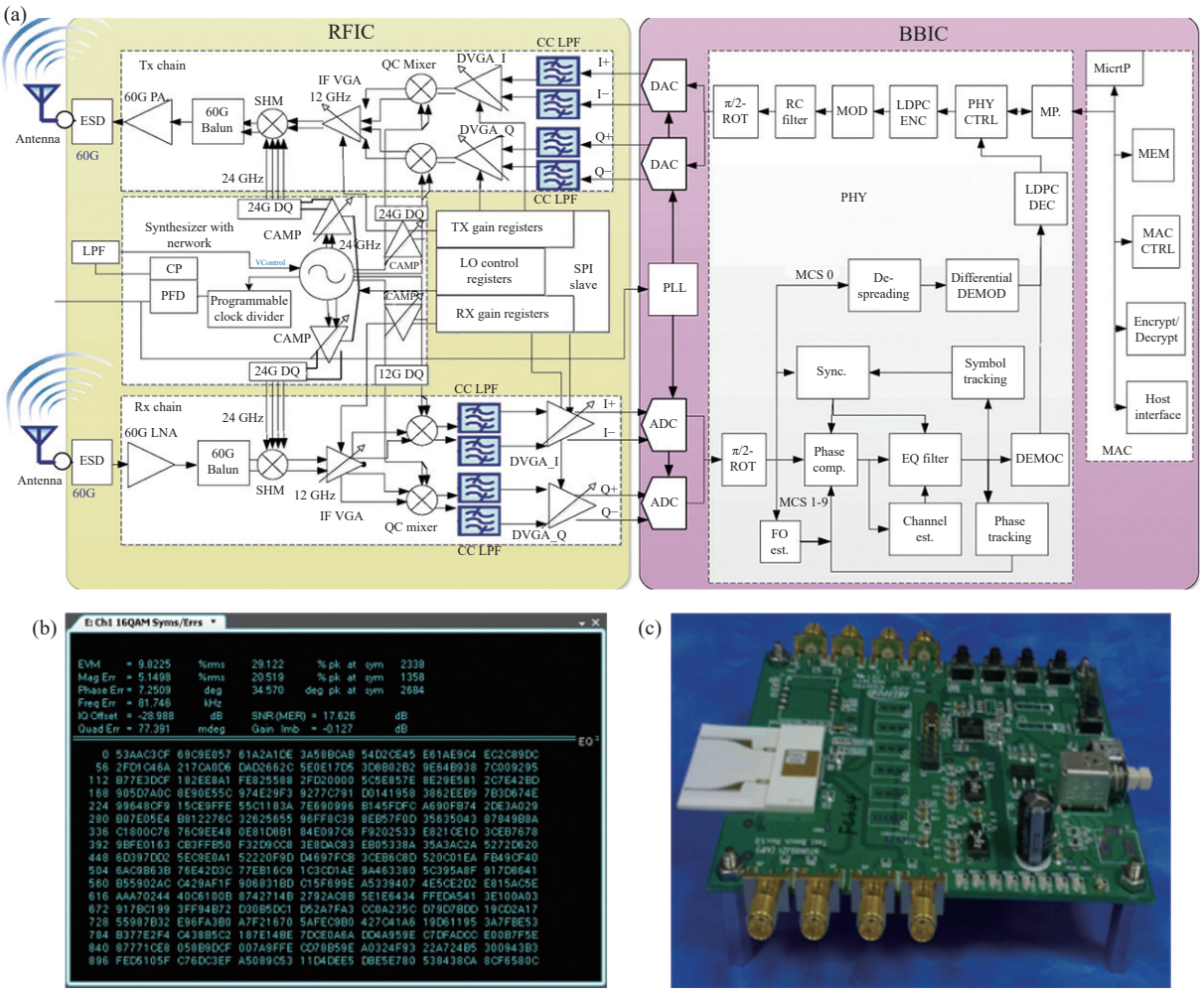

Figure 39 60 GHz dual-chip wireless communication system. (a) Block diagram; (b) EVM measurements results; (c) A photograph [11]. (ESD: electrostatic discharge. IF: intermediate frequency. QC: direct conversion. DVGA: digitally variable gain amplifier. ROT: rotator. MOD: modulation. LDPC: low density parity check. ENC: encoder. MP: modulus prescaler. MicroP: microprocessor. DEC: decoder. FO: frequency oscillator).

SISL platform, different types of low-loss and high-efficiency circuits can be designed. In reference [17], a Ka-band BPF was proposed. As shown in Figure 41, the half-wavelength resonator uses a folded structure, which not only reduces the circuit size but also forms the equal electric potential of the folded two sides of the resonator so that the electromagnetic field is distributed in the air instead of the substrate, thus reducing the dielectric loss. At the central frequency of 29.2 GHz, the IL values of the two BPFs are 0.78 dB and 1.19 dB. Compared with other state-of-the-art Ka-band BPFs, it has the advantage of low loss, which reflects the effect of regulating EM loss. A low-pass filter based on SISL was proposed in reference [18], as shown in Figure 42, and a transition using via holes is designed for ease of measurement. By using the SISL platform, the passband insertion loss is less than 1 dB at the cutoff frequency of 18 GHz.

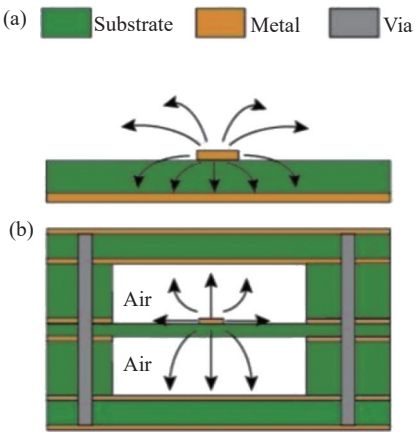

Figure 40 Cross-sectional view of (a) microstrip; (b) SISL [16].

In Figure 43, a continuous channel triplexer with multiple transmission zeros was realized based on SISL [19]. The measured insertion losses in the operating frequency bands of the three channels are 1.7, 1.5 and 1.4 dB. Due to the introduction of multiple transmission zeros, the performance of out-of-band suppression and roll-off rate of this design is improved.

Based on the self-packaged SISL technology, the slotline-based circuits have low dielectric loss and minimal ra-

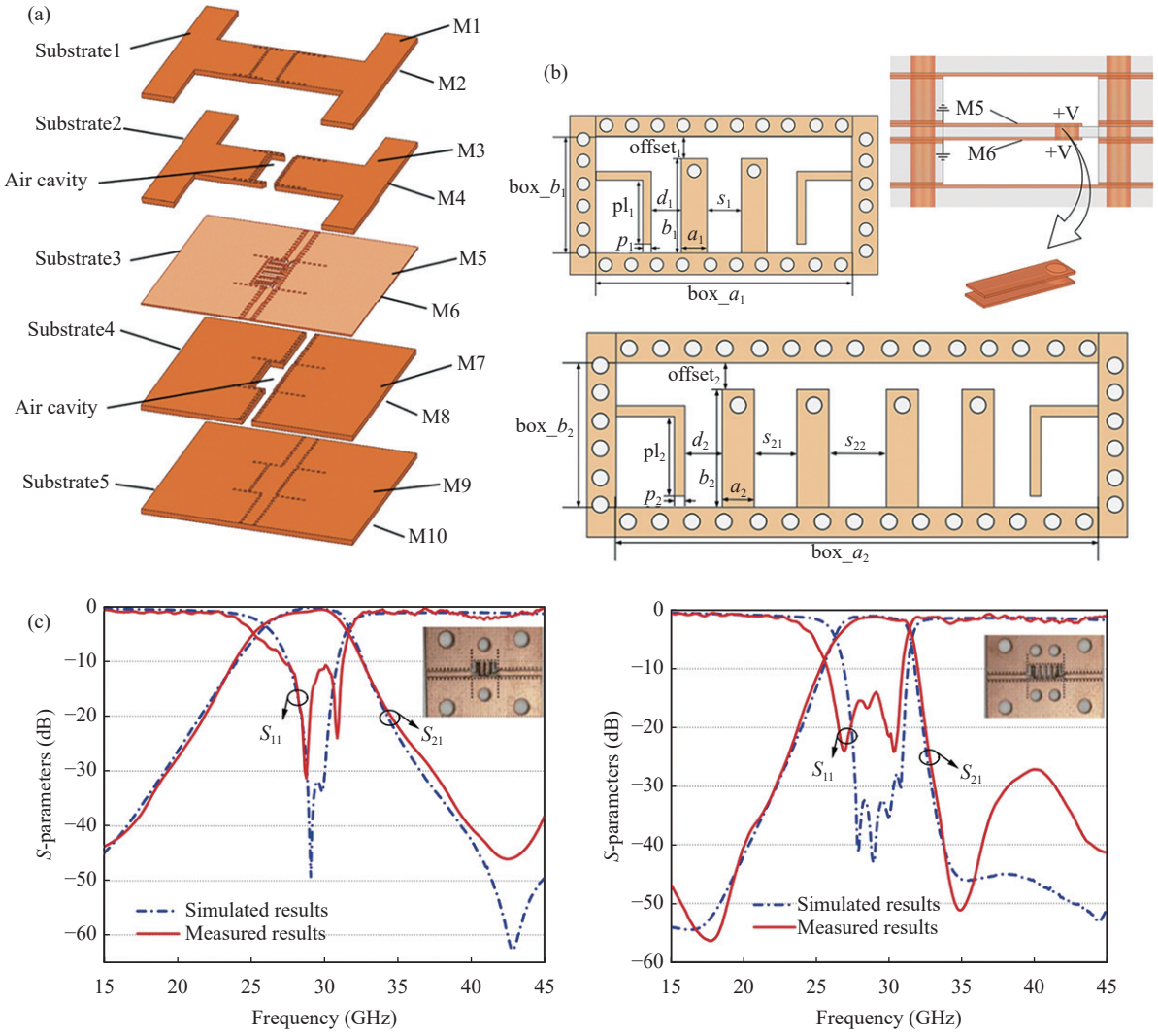

Figure 41 SISL BPFs. (a) 3-D view; (b) Top-side view of two circuits and folded resonator structure; (c) *S*-parameters of two circuits [17].

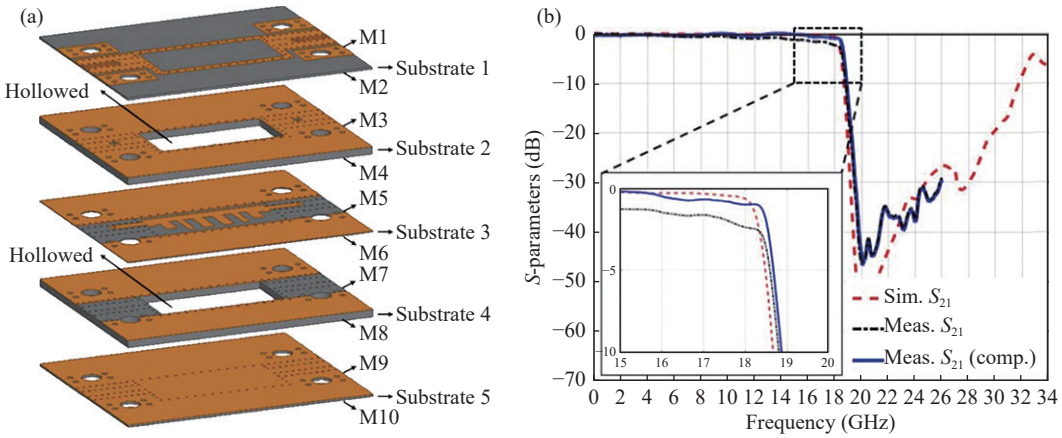

Figure 42 An SISL low-pass filter. (a) 3-D view of the low-pass filter; (b) Simulated and measured results of S_{21} [18].

diation loss. In reference [20], a magic-T was designed using a slot line on the SISL platform, as shown in Figure 44. By embedding the used slot line into the SISL and isolating it from the external space, the radiation loss of the whole circuit can be reduced. The minimum insertion loss of the proposed magic-T is 3.1 dB, and the magnitude imbalance is ±0.14 dB. In Figure 45, a differential branch-line type slot-line coupler is reported [21]. The two slot-line couplers feature low insertion loss and favorable common mode suppression.

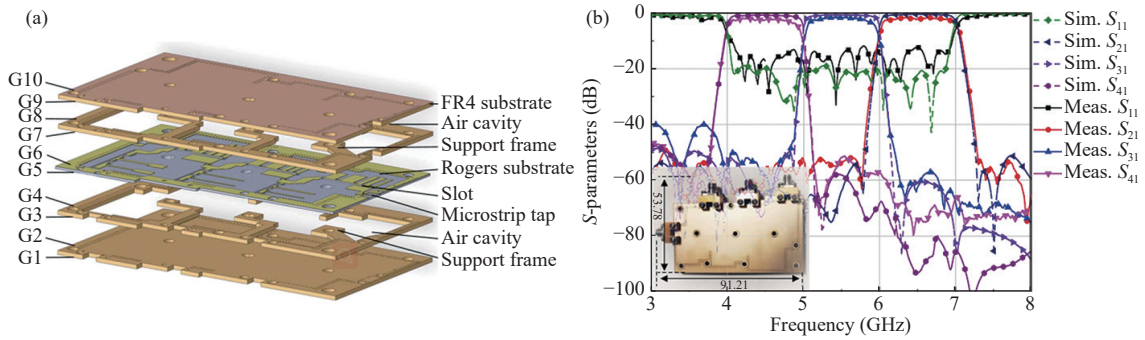

Figure 43 An SISL triplexer: (a) 3-D view; (b) *S*-parameters simulated and measured results [19].

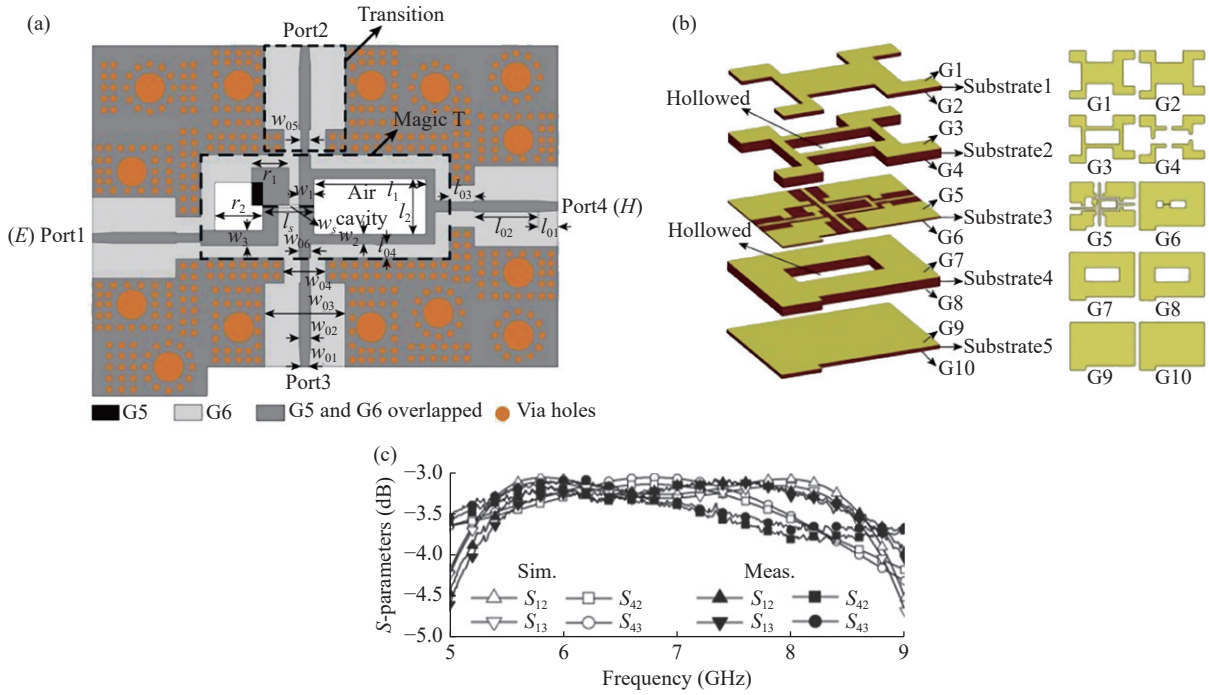

Figure 44 An SISL magic-T. (a) Top-side view of core circuit; (b) 3-D view; and (c) Simulated and measured results of S_{21} [20].

SISL technology also offers advantages in the design of active circuits with low loss and high efficiency. In reference [22], as shown in Figure 46, a 77-GHz low conversion loss (CL) fourth harmonic mixer using SISL technology was proposed. Stubs and transmission lines are used in this circuit for impedance matching. This design achieves a minimum CL of 12.2 dB. In reference [23], a filtering PA codesigned by PA and BPF based on a metal integrated substrate integrated suspended line (MI-SISL) was designed. MI-SISL offers better thermal dissipation performance

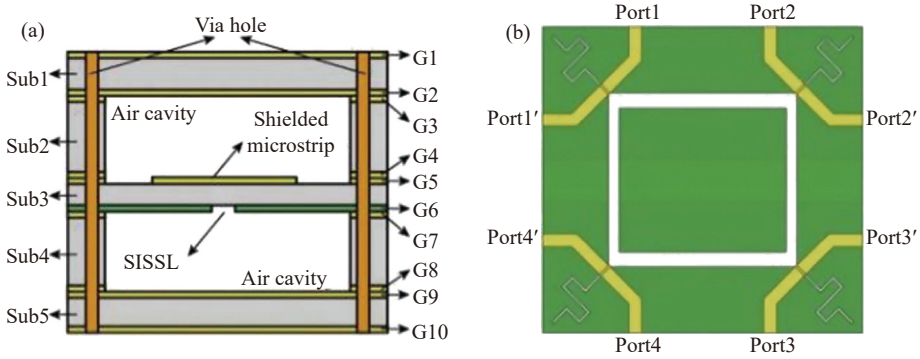

Figure 45 (to be continued)

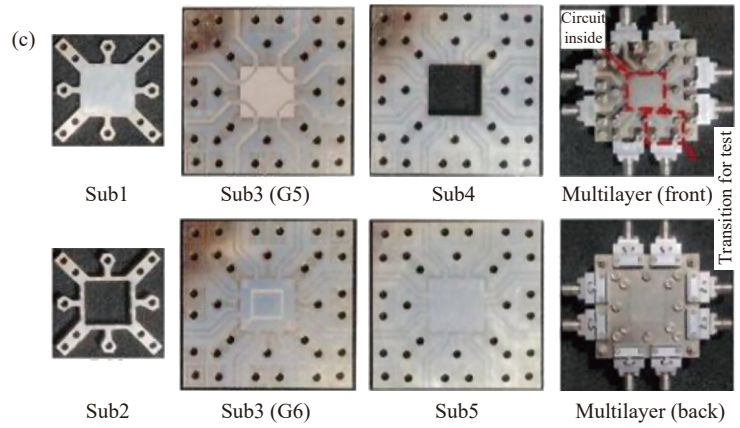

Figure 45 An SISL slot line coupler. (a) Cross-sectional view of the SISSL structure; (b) Top-side view of core circuit; (c) Photographs [21]. (Continued)

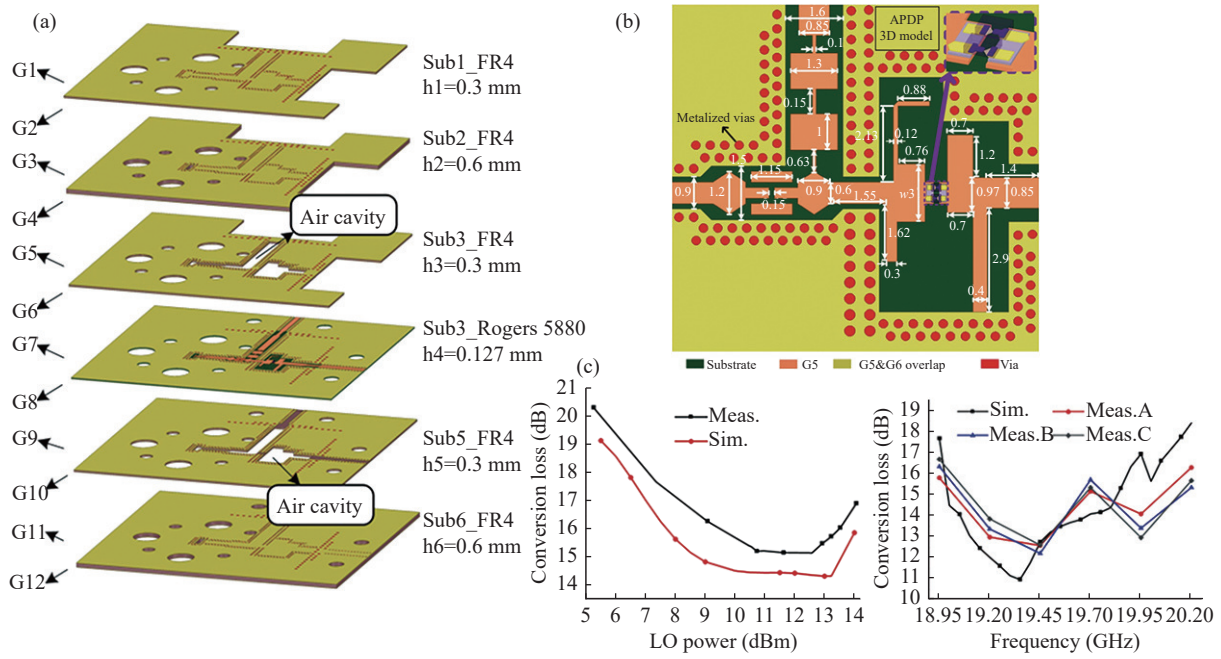

Figure 46 An SISL mixer. (a) 3-D view; (b) Top-side view of core circuit; (c) CL of the mixer [22].

than traditional SISL. Two low-pass filters are designed, with one acting as the input matching network and the other as the output matching network. The bandpass filter response and favorable harmonic suppression effect are achieved, and the harmonic suppression level up to the fifth harmonic frequency is 40 dBc. The designed power amplifier has a compact size of $0.12\lambda_g \times 0.07\lambda_g$. In terms of high-efficiency PA circuit design, Figure 47 shows a dual-band and two-state (DBDS) Doherty power amplifier (DPA) with a new design concept [24] using MI-SISL technology. Equivalent parameters of the matching part were obtained by using impedance transformation and a matched dual-band saturation point and back-off point. At 3.4/4.9 GHz, the average output power is 38/37 dBm, and the average efficiency is 37.9%/40.9%, respectively. Compared with existing dual-band DPA, DBDS DPA based on MI-SISL has a higher peak efficiency at saturation.

To further reduce the dielectric loss on the SISL platform, the DSISL [16] can be used, as shown in Figure 48(a), which helps minimize the conductor loss and dielectric loss. As shown in Figure 48(b), the dielectric loss can be minimized by partially removing the substrate according to the circuit pattern.

As shown in Figure 49, a transition from SISL to suspended coplanar waveguide (SCPW) was proposed in reference [17]. By using low-loss DSISL technology, the passband of this transition can be achieved from DC to 60 GHz. The comparison of single-metal layer, double-metal layer and double-metal layer patterned substrates shows that the double-metal layer patterned substrate has the lowest insertion loss, which reflects that the SISL platform can reduce the loss by regulating the distribution of electromagnetic waves. In reference [25], a novel 24-GHz frequency-modulated continuous wave (FMCW) radar system based on the SISL platform was proposed, which has high performance in measuring range, speed, direction, and other indoor envi-

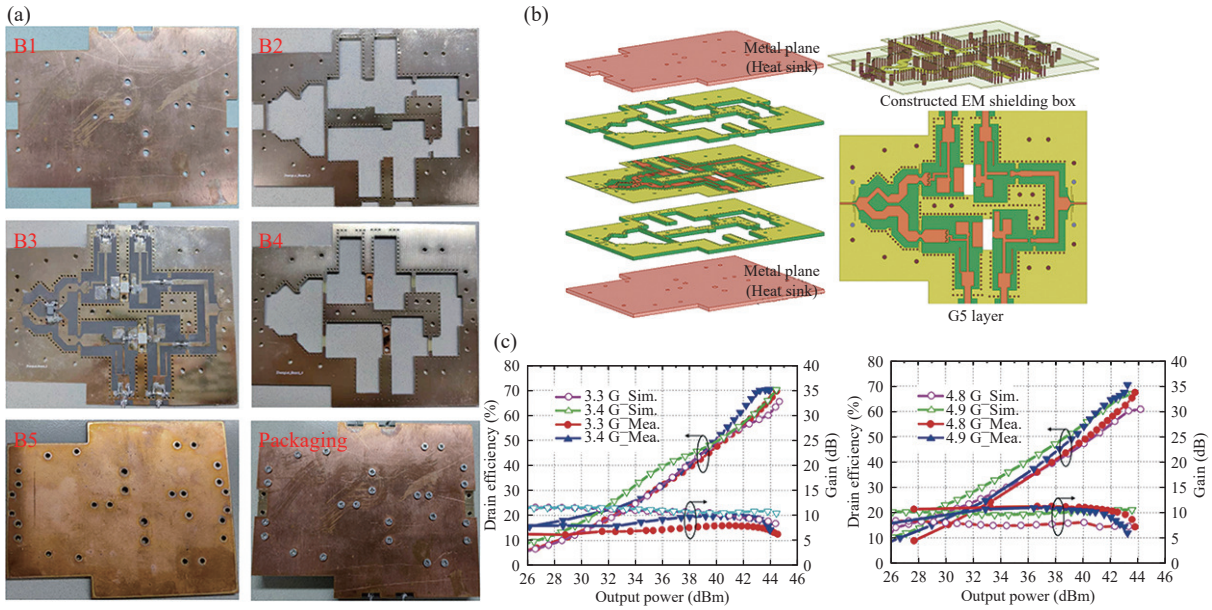

Figure 47 An SISL PA. (a) Photographs; (b) 3-D view of the proposed MI-SISL DB DPA; (c) Gains and drain efficiency versus output power of simulation and measurement in the two frequency bands [24].

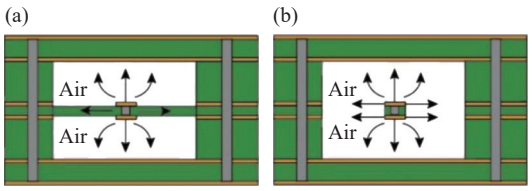

Figure 48 Cross-sectional view of (a) DSISL; (b) DSISL with patterned substrate [16].

ronments. For coupled line circuits, a loss reduction method using multiple inner layers was proposed [26], where each inner board layer is used as a transmission line layer in Figure 50. With this approach, the coupling between the coupling lines becomes that between two inner boards, and there is almost no dielectric between the two boards. Even when low-cost materials with high loss tangent are used, the dielectric loss of the core circuit remains very low. A coupled line coupler and a Marchand balun were designed using the multi-inner board SISL [26], and the insertion losses were 0.23/0.3 dB at 4.5 GHz.

The SISL platform also supports waveguide mode transmission by using patterned substrates and embedded air cavities, which show good properties, especially at higher frequency bands, such as millimeter waves. To ensure the mode conversion between quasi-TEM mode and TE_{10} mode and the transmission signal quality [27], transitions between different transmission lines in Ka-bands were designed as shown in Figure 51. All these boards were fabricated using low-cost FR4 materials. The measured data show that the insertion loss is 0.4–1.03 dB and the return loss is better than 13 dB from 26.5 GHz to 40 GHz. In ref-

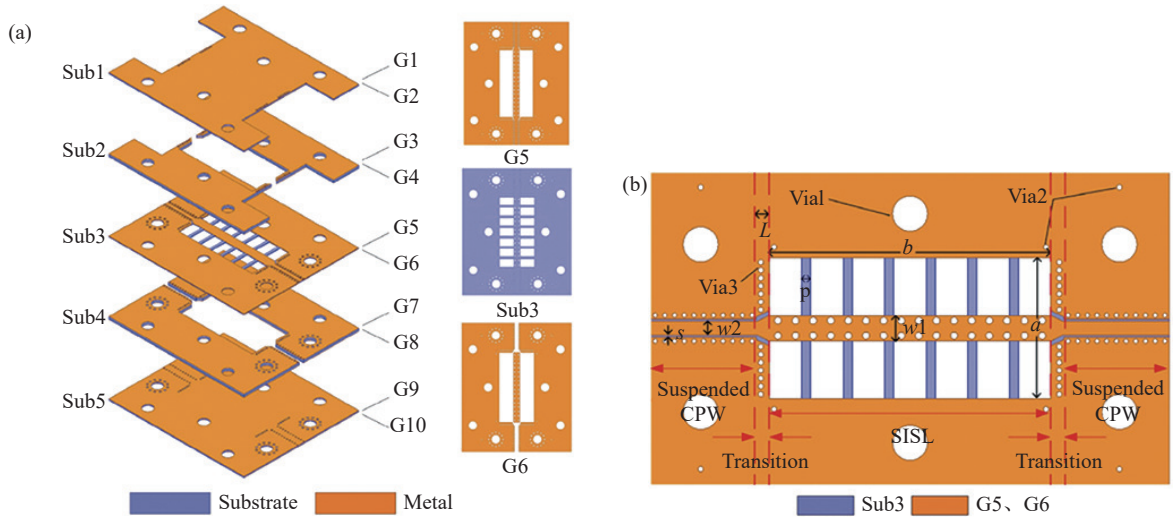

Figure 49 (to be continued)

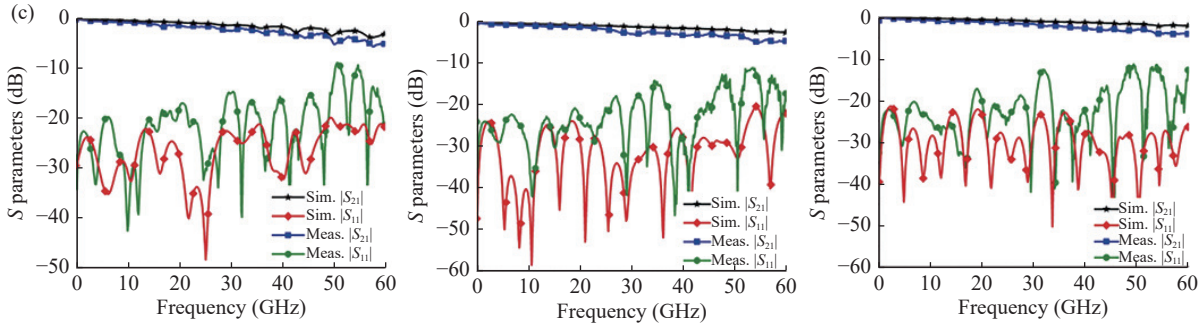

Figure 49 An SISL transition. (a) 3-D view; (b) Top view of the core circuit; (c) Comparison of the insertion loss of single-metal layer, double-metal layer and double-metal layer patterned substrates. (Continued)

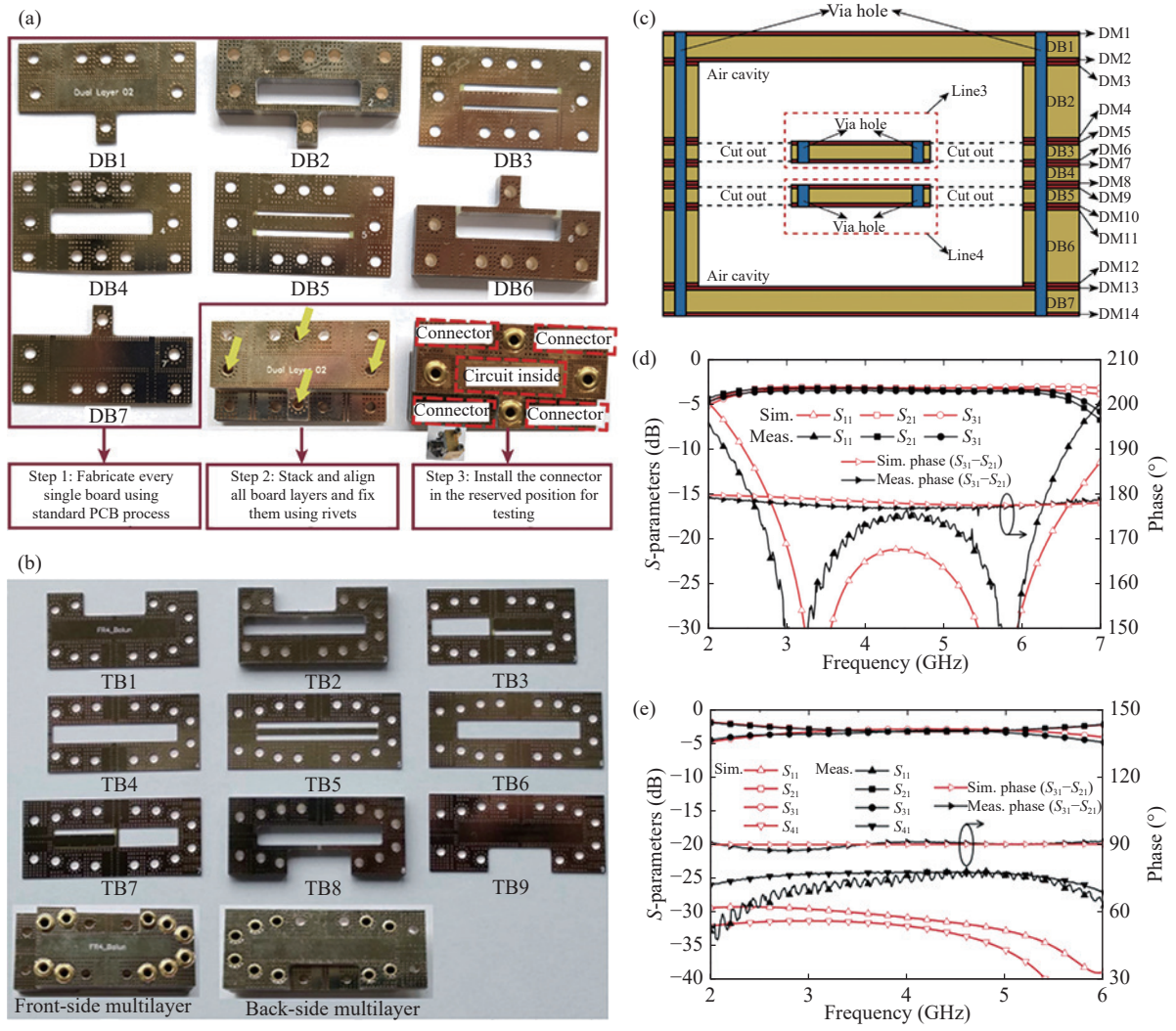

Figure 50 An SISL coupler and a Marchand balun. (a) Photographs of the SISL coupled-line coupler; (b) Photographs of the SISL Marchand balun; (c) Cross-section view of the seven-board layer SISL; (d) *S*-parameters and phase of the coupled-line coupler; (e) *S*-parameters and phase of the Marchand balun [26].

erence [28], a 1:4 Ka-band SISL power divider was designed, as shown in Figure 52. To obtain better matching in broadband, the iris structure is used at the T-junction between the SISL and the air-filled SIW, and a bandwidth of 61.7% is obtained. In addition, adding three ports to the load resistors increases the isolation of the overall design from 2.5 dB to 15 dB. In summary, the SISL platform offers advantages in reducing dielectric loss and can also reduce metal loss and radiation loss of circuits. Some case studies are reported in reference [29]. The loss reduction of

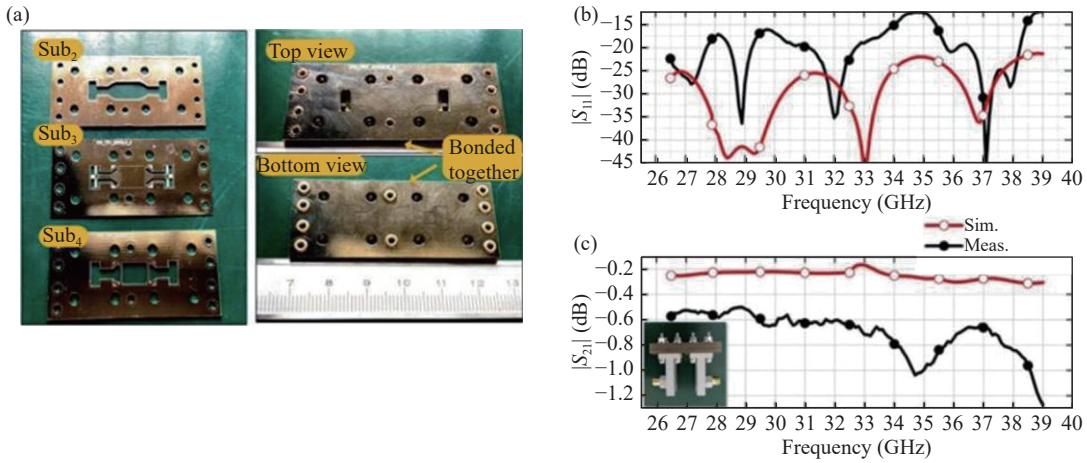

Figure 51 An SISL transition. (a) Photographs of the SISL transition; (b)(c) *S*-parameters of the transition [27].

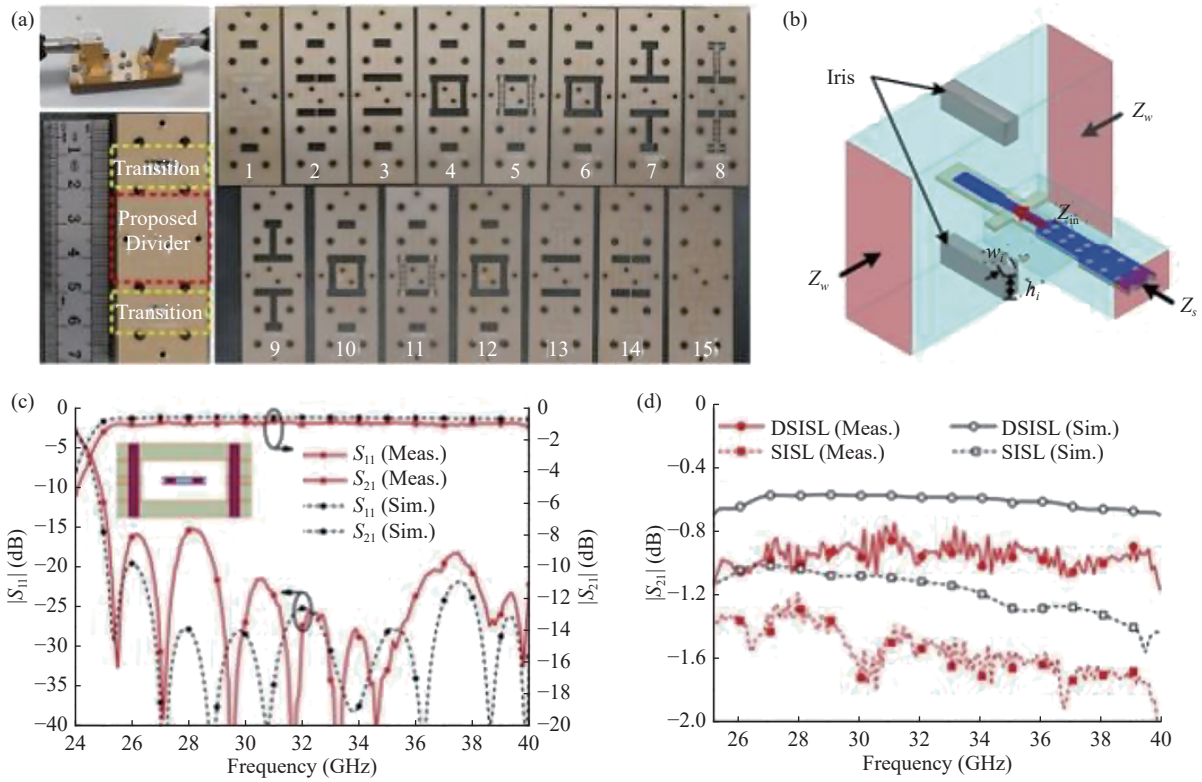

Figure 52 An SISL power divider. (a) Photographs of SISL power divider; (b) T-junction; (c) *S*-parameters of the back-to-back power divider with transitions using DSISL; (d) Insertion loss comparison of two back-to-back power dividers with transitions [28].

the SISL platform is significant in the millimeter wave frequency band .

The use of an air cavity will reduce loss, but it will reduce the equivalent dielectric constant, which introduces challenges to miniaturization. The design of the SISL quasilumped element circuit makes full use of the advantages of multiple layers to realize circuit miniaturization. In Figure 53, the spiral inductor was modeled on the SISL platform, and the Q factor was also enhanced by using double metal layers and a patterned substrate [16].

Based on the SISL platform, a compensated interdigital capacitor (CIDC) model was established, as shown in Figure 54 [30]. Compared with the traditional single-layer interdigital and flat plate capacitor, the CIDC fully uses the horizontal and vertical electric fields and increases the capacitance density. Using the CIDC, a compact lumped balun is designed, and the core size is $0.06\lambda_g \times 0.11\lambda_g$. As shown in Figure 55, miniaturized 5G SISL BPFs were proposed [31]. By using differential inductors as resonators, the BPF size can be reduced. The circuit sizes of the designed 2nd- and 4th-order filters are only $0.0023\lambda_g^2$ and $0.0052\lambda_g^2$, respectively.

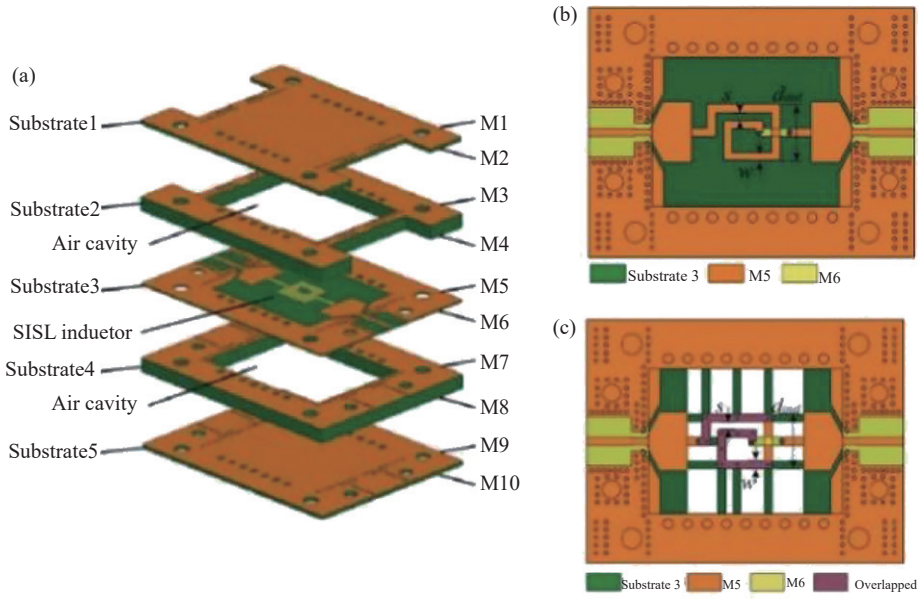

Figure 53 An SISL spiral inductor. (a) 3-D-view; (b) Top view of the SISL inductor without patterned substrate; and (c) With patterned substrate [16].

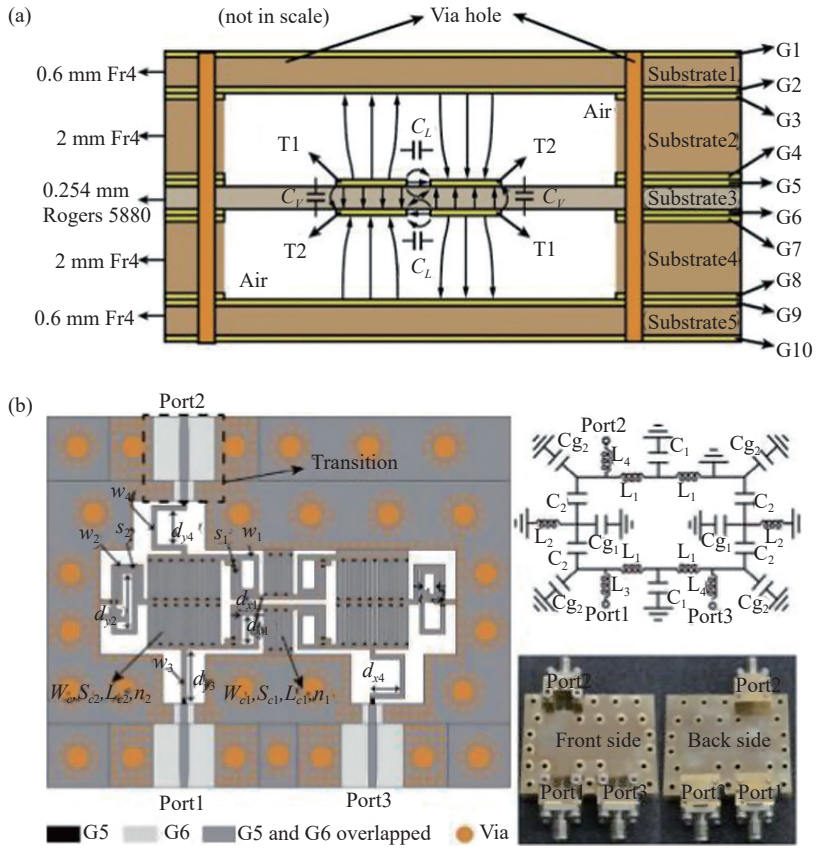

Figure 54 An SISL balun. (a) Cross-sectional view of the proposed SISL balun; (b) Core circuit, equivalent circuit and photograph of the SISL lumped balun [30].

2. Cavities with embedded medium and circuits

For further miniaturization of the circuit, the SISL structure takes advantage of the embedded cavity. Dielectric blocks with high dielectric constants can be loaded into the cavity, which improves the miniaturization level of the circuit.

A high-density SISL capacitor using a filled dielectric block is reported, as shown in Figure 56 [32]. Because two air cavities are were formed due to the excavation in Sub2 and Sub4, by filling these cavities with dielectric blocks, the equivalent dielectric constant of the overall design in-

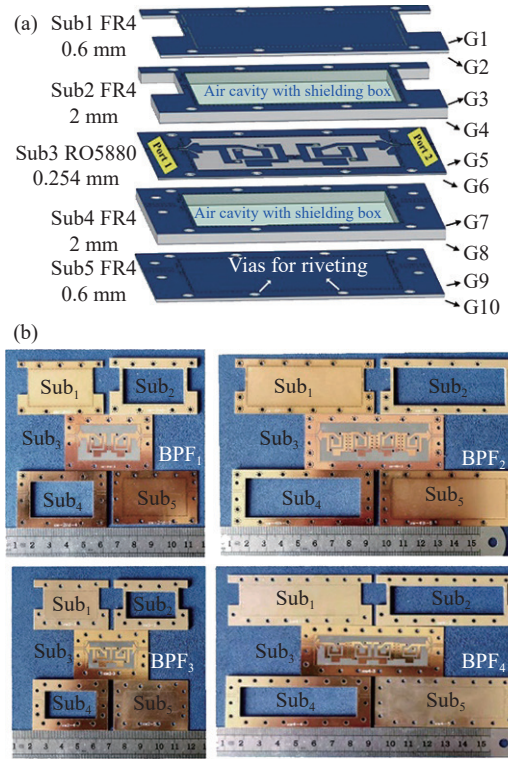

Figure 55 Miniaturized SISL BPFs. (a) 3-D view; (b) Photographs of four BPFs [31].

creased, which improved the capacitance value of the capacitor. Specifically, a ceramic dielectric block with a permittivity of 38.3 was filled in the air cavity. The results show that the extracted equivalent capacitance can reach 29 pF, and the capacitance density can reach 0.067 pF/mm^3. A lumped LPF was designed using the dielectric-filled capacitor, and the main circuit size was only $0.005\lambda_g \times 0.013\lambda_g$. The design has a clear miniaturization advantage compared to competing state-of-the-art approaches.

The filled dielectric block can also be used as a resonator for filter design. Figure 57 shows an SISL-based dual-band dielectric resonator filter (DRF) [33]. The DRF was fed by a strip ring and achieved degenerate mode coupling through a coupling ring. The filter used multimode dielectric resonators to generate two passbands and four out-of-band transmission zeros through the designed coupling path. The size of this filter is 38.4 mm × 19 mm × 3.8 mm.

3. Composite metasubstrates and circuits

EM waves can be regulated by meta-substrates, which can enhance circuit performance. With periodic arrangement of the metasubstrate, high permittivity can be obtained, which contributes to circuit miniaturization. SISL-based metasurfaces with a high permittivity have been reported, as shown in Figure 58 [34]. Their main circuit is implemented on Substrate3 with the metasubstrate below. The "I-shaped" element was designed under Substrate3 as a metasubstrate. A high relative permittivity of 17.25 is achieved. A Gysel power divider (PD) was designed by using an SISL-based metasubstrate. Figure 59 shows the Gysel PD with a compact circuit size of $0.15\lambda_g \times 0.27\lambda_g$, which achieves a size reduction of 61% compared to the conventional counterpart.

V. Conclusion

This article presents several kinds of circuit designs using electromagnetic control technology in the radio frequency band. The separation of magnetic and electric coupling paths contributes greatly to the design of filters in microwave communication. The regulation of electromagnetic energy is a valuable tool when designing oscillators, VCOs, PAs, ILFDs, and SPDTs with excellent performance. The principle of regulating the airspace electromagnetic field has been greatly applied in circuit designs, including filters, couplers, LNAs, PAs, and metasubstrates based on the SISL platform. These circuits demonstrate that the development and application of techniques for regulating the electromagnetic field can improve the circuit performance in terms of flexible control of TZs, loading effect for size reduction, low insertion loss, improved selectivity, low

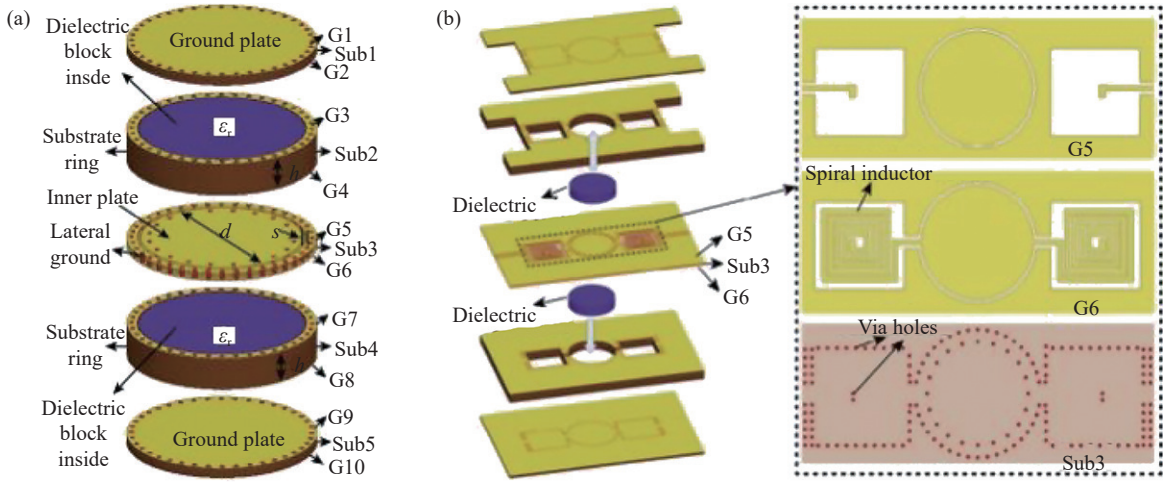

Figure 56 An SISL low-pass filter using dielectric filled capacitor. (a) 3D-view of dielectric filled capacitor and (b) SISL LPF using dielectric filled capacitor [32].

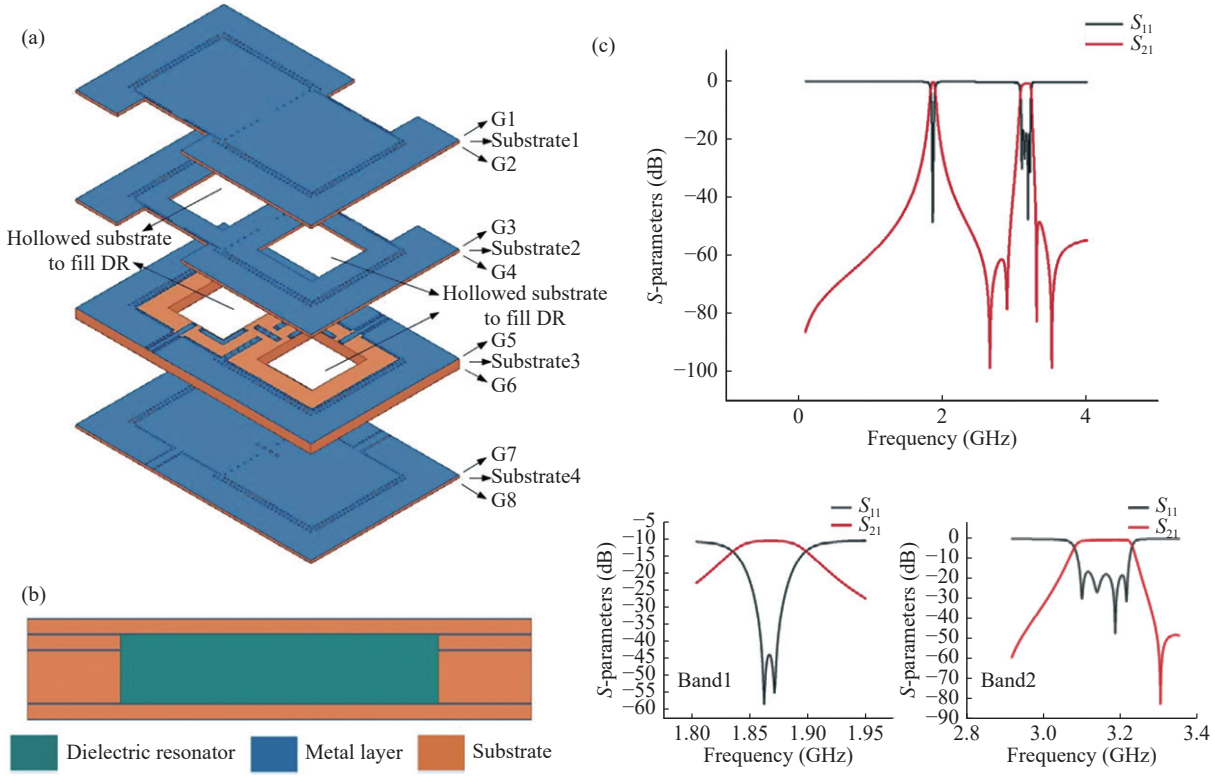

Figure 57 An SISL dielectric resonator filter. (a) 3D-view; (b) Cross-section view of the dielectric resonator; (c) S-parameters [33].

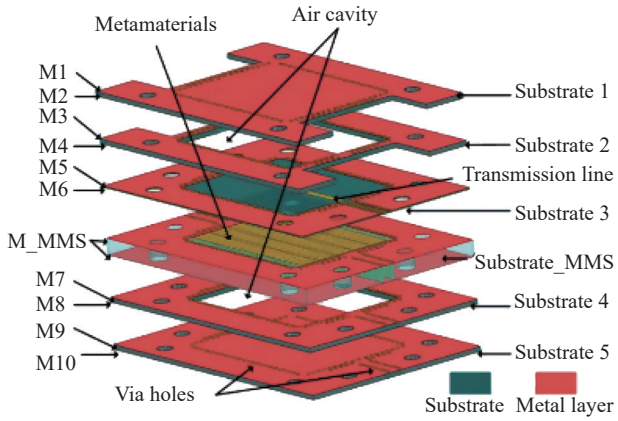

Figure 58 The implementation of metasubstrates on SISL [34].

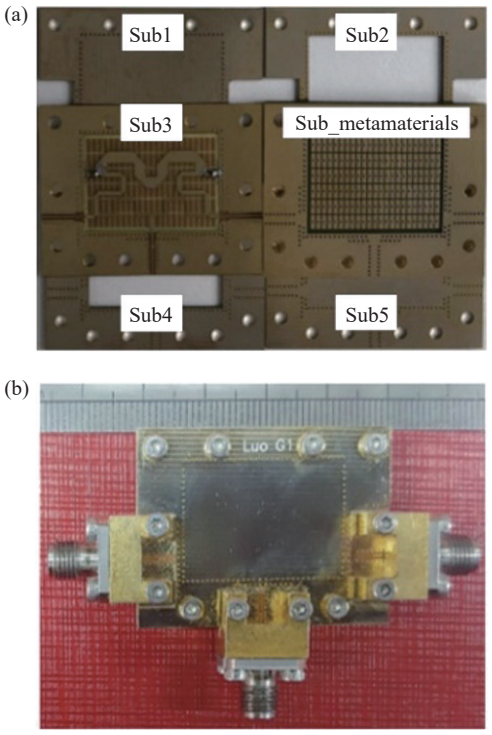

Figure 59 An SISL Gysel PD. (a) Photographs of each substrate; (b) Photographs of packaged PD [34].

phase noise, high Q, high efficiency, and size reduction.

Acknowledgment

This work was supported in part by the National Natural Science Foundation of China for Key Project (Grant No. 61831017), the General Project (Grant No. 61471092), the Distinguished Young Scholar (Grant No. 61625105), and the National Key R&D Program of China (Grant No. 2018YFB2202500).

The author would like to thank Yongqiang Wang, Yi Wu, Fanyi Meng, Ningning Yan, Qingling Zhang, Zehua Yue, Mingyun Liu, Peiyang Wang, Jianteng Yang, Yongyun Wang, Yufeng Ding, and Haoyue Jiang for their valuable support to this work.

References

[1] K. X. Ma, J. G. Ma, K. S. Yeo, *et al*., "A compact size coupling controllable filter with separate electric and magnetic coupling paths," *IEEE Transactions on Microwave Theory and Techniques*,

vol. 54, no. 3, pp. 1113–1119, 2006.
[2] K. X. Ma, N. Mahalingam, S. X. Mou, *et al*., "Integrated circuit architecture with strongly coupled LC tanks," *Patent*, 09331659(B2), US, 2016-05-03.
[3] K. X. Ma, S. X. Mou, and K. S. Yeo, "A miniaturized millimeter-wave standing-wave filtering switch with high P1dB," *IEEE Transactions on Microwave Theory and Techniques*, vol. 61, no. 4, pp. 1505–1515, 2013.
[4] K. X. Ma, T. B. Kumar, and K. S. Yeo, "A reconfigurable K-/Ka-band power amplifier with high PAE in 0.18-μm SiGe BiCMOS for multi-band applications," *IEEE Transactions on Microwave Theory and Techniques*, vol. 63, no. 12, pp. 4395–4405, 2015.
[5] K. X. Ma, Q. Zou, F. Y. Meng, *et al*., "Generalized multiple coupled tanks for silicon based RF/mm-wave IC (Invited)," in *2015 Asia-Pacific Microwave Conference (APMC)*, Nanjing, China, pp.1–3, 2015.
[6] J. A. Han, Z. H. Kong, K. X. Ma, *et al*., "A 26.8 dB gain 19.7 dBm CMOS power amplifier using 4-way hybrid coupling combiner," *IEEE Microwave and Wireless Components Letters*, vol. 25, no. 1, pp. 43–45, 2015.
[7] F. Y. Meng, K. X. Ma, and K. S. Yeo, "A 130-to-180 GHz 0.0035 mm^2 SPDT switch with 3.3 dB loss and 23.7 dB isolation in 65 nm bulk CMOS," in *2015 IEEE International Solid-State Circuits Conference*, San Francisco, CA, USA, pp.1–3, 2015.
[8] N. Mahalingam, K. X. Ma, K. S. Yeo, *et al*., "Coupled dual LC tanks based ILFD with low injection power and compact size," *IEEE Microwave and Wireless Components Letters*, vol. 24, no. 2, pp. 105–107, 2014.
[9] Z. P. Wang, K. X. Ma, Z. L. Ma, *et al*., "A 20.7–43.8-GHz low power reconfigurable ×2/×3 frequency multiplier for multiple 5G-mm-wave bands," *IEEE Journal of Solid-State Circuits*, vol. 57, no. 8, pp. 2348–2361, 2022.
[10] X. L. Liu and H. C. Luong, "A fully integrated 0.27-thz injection-locked frequency synthesizer with frequency-tracking loop in 65-nm CMOS," *IEEE Journal of Solid-State Circuits*, vol. 55, no. 4, pp. 1051–1063, 2020.
[11] K. X. Ma, S. X. Mou, N. Mahalingam, *et al*., "An integrated 60GHz low power two-chip wireless system based on IEEE802.11ad standard," in *2014 IEEE MTT-S International Microwave Symposium (IMS2014)*, Tampa, FL, USA, pp.1–4, 2014.
[12] K. X. Ma and K. T. Chan, "Quasi-planar circuits with air cavities," *Patent*, 2007149046, Singapore, 2007-12-27.
[13] K. X. Ma, N. N. Yan, and Y. Q. Wang, "Recent progress in SISL circuits and systems: Review of passive and active circuits demonstrating SISL's low loss and self-packaging and showcasing the merits of metallic, shielded, suspended lines," *IEEE Microwave Magazine*, vol. 22, no. 4, pp. 49–71, 2021.
[14] F. Parment, A. Ghiotto, T. P. Vuong, *et al*., "Air-filled substrate integrated waveguide for low-loss and high power-handling millimeter-wave substrate integrated circuits," *IEEE Transactions on Microwave Theory and Techniques*, vol. 63, no. 4, pp. 1228–1238, 2015.
[15] M. D. Fernandez, J. A. Ballesteros, and A. Belenguer, "Design of a hybrid directional coupler in empty substrate integrated waveguide (ESIW)," *IEEE Microwave and Wireless Components Letters*, vol. 25, no. 12, pp. 796–798, 2015.
[16] L. Y. Li, K. X. Ma, and S. X. Mou, "Modeling of new spiral inductor based on substrate integrated suspended line technology," *IEEE Transactions on Microwave Theory and Techniques*, vol. 65, no. 8, pp. 2672–2680, 2017.
[17] X. Wu, K. X. Ma, Y. Q. Wang, *et al*., "An FR4-based dc to 60 GHz substrate integrated suspended line to suspended coplanar waveguide transition," *Microwave and Optical Technology Letters*, vol. 64, no. 2, pp. 203–207, 2022.
[18] J. W. McDaniel, S. Saeedi, M. B. Yeary, *et al*., "A low-loss fully board-integrated low-pass filter using suspended integrated stripline technology," *IEEE Transactions on Components, Packaging and Manufacturing Technology*, vol. 8, no. 11, pp. 1948–1955, 2018.
[19] L. G. Zhou, Z. H. Long, Q. Y. Feng, *et al*., "Channel-Continuous triplexer with multiple transmission zeros based on cascaded high-pass and low-pass filters," *IEEE Microwave and Wireless Components Letters*, vol. 32, no. 5, pp. 395–398, 2022.
[20] Y. Q. Wang, K. X. Ma, and S. X. Mou, "A low-loss self-packaged magic-T with compact size using SISL technology," *IEEE Microwave and Wireless Components Letters*, vol. 28, no. 1, pp. 13–15, 2018.
[21] Y. Q. Wang, M. Yu, and K. X. Ma, "Substrate integrated suspended slot line and its application to differential coupler," *IEEE Transactions on Microwave Theory and Techniques*, vol. 68, no. 12, pp. 5178–5189, 2020.
[22] N. Zhang, K. X. Ma, Y. Q. Wang, *et al*., "A 77-GHz low-conversion-loss fourth-harmonic mixer on SISL Platform," *IEEE Microwave and Wireless Components Letters*, vol. 32, no. 6, pp. 567–570, 2022.
[23] T. Feng, K. X. Ma, Y. Q. Wang, *et al*., "Bandpass-filtering power amplifier with compact size and wideband harmonic suppression," *IEEE Transactions on Microwave Theory and Techniques*, vol. 70, no. 2, pp. 1254–1268, 2022.
[24] L. Zhang, K. X. Ma, H. P. Fu, *et al*., "A dual-band and dual-state Doherty power amplifier using metal-integrated and substrate-integrated suspended line technology," *IEEE Transactions on Microwave Theory and Techniques*, vol. 70, no. 1, pp. 402–415, 2022.
[25] B. D. Liu, K. X. Ma, Y. Q. Wang, *et al*., "An SISL-based 24-GHz FMCW radar with self-packaged six-port butler matrix receiver," *IEEE Transactions on Components, Packaging and Manufacturing Technology*, vol. 12, no. 10, pp. 1661–1672, 2022.
[26] Y. Q. Wang, K. X. Ma, and Ming Yu, "A low-cost substrate integrated suspended line platform with multiple inner boards and its applications in coupled-line circuits," *IEEE Transactions on Components, Packaging and Manufacturing Technology*, vol. 10, no. 12, pp. 2087–2098, 2020.
[27] W. Xu, K. X. Ma, S. S. Xu, *et al*., "*Ka*-Band SISL-to-AFSIW transitions with fabrication tolerance characteristics," *IEEE Transactions on Components, Packaging and Manufacturing Technology*, vol. 9, no. 10, pp. 2097–2103, 2019.
[28] Z. Y. Qin, K. X. Ma, N. N. Yan, *et al*., "An FR4-Based self-packaged full *Ka*-Band low-loss 1: 4 power divider using SISL to air-filled SIW T-Junction," *IEEE Transactions on Components, Packaging and Manufacturing Technology*, vol. 12, no. 3, pp. 587–590, 2022.
[29] Y. Q. Wang and K. X. Ma, "Loss mechanism of the SISL and the experimental verifications," *IET Microwaves, Antennas & Propagation*, vol. 13, no. 11, pp. 1768–1772, 2019.
[30] Y. Q. Wang, K. X. Ma, and S. X. Mou, "A compact SISL balun using compensated interdigital capacitor," *IEEE Microwave and Wireless Components Letters*, vol. 27, no. 9, pp. 797–799, 2017.
[31] X. Wei, K. X. Ma, and Y. X. Guo, "Design of miniaturized 5G SISL BPFs with wide stopband using differential drive inductor resonators," *IEEE Transactions on Microwave Theory and Techniques*, vol. 70, no. 6, pp. 3115–3124, 2022.
[32] Y. Q. Wang, M. Yu, and K. X. Ma, "A compact low-pass filter using dielectric-filled capacitor on SISL platform," *IEEE Microwave and Wireless Components Letters*, vol. 31, no. 1, pp. 21–24, 2021.
[33] W. K. Chu and K. X. Ma, "Design of dual-band dielectric resonator filter based on substrate integrated suspended line," in *2021 IEEE 4th International Conference on Electronics Technology (ICET)*, , Chengdu, China, pp.264–268, 2021.
[34] J. J. Luo, H. P. Fu, K. X. Ma, *et al*., "A miniaturized and self-packaged Gysel power divider with embedded metamaterials in SISL platform," *IEICE Electronics Express*, vol. 18, no. 12, article no. 20210196, 2021.
[35] J. S. Hong and M. J. Lancaster, *Microstrip Filters for RF/Microwave Applications*. John Wiley & Sons, Inc. , New York, NY, USA, pp.244–245, 2001.
[36] K. X. Ma, K. S. Yeo, J. G. Ma, *et al*., "An ultra-compact hairpin band pass filter with additional zero points," *IEEE Microwave and Wireless Components Letters*, vol. 17, no. 4, pp. 262–264, 2007.
[37] Q. X. Chu and H. Wang, "A compact open-loop filter with mixed

electric and magnetic coupling," *IEEE Transactions on Microwave Theory and Techniques*, vol. 56, no. 2, pp. 431–439, 2008.
[38] H. Wang and Q. X. Chu, "An EM-coupled triangular open-loop filter with transmission zeros very close to passband," *IEEE Microwave and Wireless Components Letters*, vol. 19, no. 2, pp. 71–73, 2009.
[39] W. Xu, K. X. Ma, and C. Y. Du, "Design and loss reduction of multiple-zeros dual-band bandpass filter using SISL," *IEEE Transactions on Circuits and Systems II:Express Briefs*, vol. 68, no. 4, pp. 1168–1172, 2021.
[40] Y. T. Chu, K. X. Ma, Y. Q. Wang, *et al*., "A self-packaged low-loss and compact SISL DBBPF with multiple TZs," *IEEE Microwave and Wireless Components Letters*, vol. 29, no. 3, pp. 192–194, 2019.
[41] W. W. Zhang, K. X. Ma, H. Zhang, *et al*., "Design of a com-pact SISL BPF with SEMCP for 5G Sub-6 GHz bands," *IEEE Microwave and Wireless Components Letters*, vol. 30, no. 12, pp. 1121–1124, 2020.
[42] H. Zhang, K. X. Ma, W. W. Zhang, *et al*., "A novel self-packaged DBBPF with multiple TZs for 5G sub-6 GHz applications," *Microwave and Optical Technology Letters*, vol. 65, no. 1, pp. 62–68, 2023.
[43] F. Y. Meng, K. X. Ma, S. S. Xu, *et al*., "Design of quarter-wavelength resonator filters with coupling controllable paths," in *2012 IEEE Asia Pacific Conference on Circuits and Systems*, Kaohsiung, China, pp.248–251, 2012.
[44] H. Wang and Q. X. Chu, "An inline coaxial quasi-elliptic filter with controllable mixed electric and magnetic coupling," *IEEE Transactions on Microwave Theory and Techniques*, vol. 57, no. 3, pp. 667–673, 2009.
[45] F. C. Chen, J. M. Qiu, S. W. Wong, *et al*., "Dual-Band coaxial cavity bandpass filter with helical feeding structure and mixed coupling," *IEEE Microwave and Wireless Components Letters*, vol. 25, no. 1, pp. 31–33, 2015.
[46] F. C. Chen, H. T. Hu, J. M. Qiu, *et al*., "Cascaded triplet filter using mixed electric and magnetic coupling structure with wide stopband performance," *Microwave and Optical Technology Letters*, vol. 56, no. 12, pp. 2937–2940, 2014.
[47] K. Gong, W. Hong, Y. Zhang, *et al*., "Substrate integrated waveguide quasi-elliptic filters with controllable electric and magnetic mixed coupling," *IEEE Transactions on Microwave Theory and Techniques*, vol. 60, no. 10, pp. 3071–3078, 2012.
[48] S. Sirci, M. Á. Sánchez-Soriano, J. D. Martínez, *et al*., "Design and multiphysics analysis of direct and cross-coupled SIW combline filters using electric and magnetic couplings," *IEEE Transactions on Microwave Theory and Techniques*, vol. 63, no. 12, pp. 4341–4354, 2015.
[49] M. Dong, D. Y. Shen, C. J. Ma, *et al*., "A cascaded six order bandpass siw filter using electric and magnetic couplings technology," in *2017 Sixth Asia-Pacific Conference on Antennas and Propagation (APCAP)*, Xi'an, China, pp.1–3, 2017.
[50] L. Szydlowski, A. Lamecki, and M. Mrozowski, "Coupled-resonator filters with frequency-dependent couplings: Coupling matrix synthesis," *IEEE Microwave and Wireless Components Letters*, vol. 22, no. 6, pp. 312–314, 2012.
[51] Y. X. He, G. Macchiarella, Z. W. Ma, *et al*., "Advanced direct synthesis approach for high selectivity in-line topology filters comprising N - 1 adjacent frequency-variant couplings," *IEEE Access*, vol. 7, pp. 41659–41668, 2019.
[52] J. S. Chen and A. M. Niknejad, "A compact 1 V 18.6 dBm 60 GHz power amplifier in 65 nm CMOS," in *2011 IEEE International Solid-State Circuits Conference*, San Francisco, CA, USA, pp.432–433, 2011.
[53] Z. M. Chen, C. C. Wang, H. C. Yao, *et al*., "A BiCMOS W-band 2×2 focal-plane array with on-chip antenna," *IEEE Journal of Solid-State Circuits*, vol. 47, no. 10, pp. 2355–2371, 2012.
[54] N. Mahalingam, K. X. Ma, K. S. Yeo, *et al*., "*K*-band high-PAE wide-tuning-range VCO using triple-coupled *LC* tanks," *IEEE Transactions on Circuits and Systems II:Express Briefs*, vol. 60, no. 11, pp. 736–740, 2013.
[55] Q. Zou, K. X. Ma, and K. S. Yeo, "A low phase noise and wide tuning range millimeter-wave VCO using switchable coupled VCO-cores," *IEEE Transactions on Circuits and Systems I:Regular Paper*, vol. 62, no. 2, pp. 554–563, 2015.
[56] D. M. Pozar, *Microwave Engineering*, 4th ed. , John Wiley & Sons, 111 River Street, Hoboken, NJ, USA, pp.147–153, 2011.

Kaixue Ma received the B.E. and M.E. degrees from Northwestern Polytechnical University (NWPU), Xi'an, China, and Ph.D. degree from Nanyang Technological University (NTU), Singapore. From 1997 to 2002, he worked at the Chinese Academy of Space Technology (Xi'an) as a group leader. From 2005 to 2007, he was with MEDs Technologies as an R&D Manager. From 2007 to 2010, he was with the Singapore-based publicly listed company ST Electronics as an R&D manager, project leader, technique management committee and technique consultant in 2011. From 2010 to 2013, he was with NTU as a Senior Research Fellow and Millimeter-wave RFIC team leader for the 60-GHz Flagship Chipset project. From 2013 to 2018, he was a Full Professor at the University of Electronic Science and Technology of China (UESTC), Chengdu, China. Since Feb. 2018, he has been the Dean and Distinguished Professor of the School of Microelectronics at Tianjin University, the Director of Tianjin Key Laboratory of Imaging and Sensing Microelectronics Technology and the Chairperson of Tianjin IC Association. Dr. Ma proposed a variety of RF and microwave integrated circuits based on advanced CMOS, SiGe BiCMOS, GaAs and SOI technologies, and microwave circuit and system design technology patented with "quasiplanar circuits with embedded air cavity" named SISL in publication. He was responsible for designing the first low-power reconfigurable 60 GHz SiGe millimeter-wave transceiver SOC, packaging and system testing and completed a high-speed dual-chip wireless communication system. He is currently working on GaAs and silicon-based RF millimeter-wave and THz integrated circuits and systems for wireless communication and sensor applications. He has filed 40 patents, published two books, over 170 IEEE journal articles and 190 international conference papers.

Dr. Ma is Fellow of Chinese Institute of Electronics and awardee of the Chinese National Science Fund for Distinguished Young Scholars. He received 10 technique awards, including the best paper award. He was Associate Editor for the *IEEE Transactions on Microwave Theory and Techniques* and Guest Editor of *IEEE Microwave Magazine* and a current member and organizer for international conferences. He was the Coordinator IEEE MTT-S R10 for China and Singapore from 2016 to 2022 and current member and Speakers Bureau of MTT-4, etc. (Email: makaixue@tju.edu.cn)